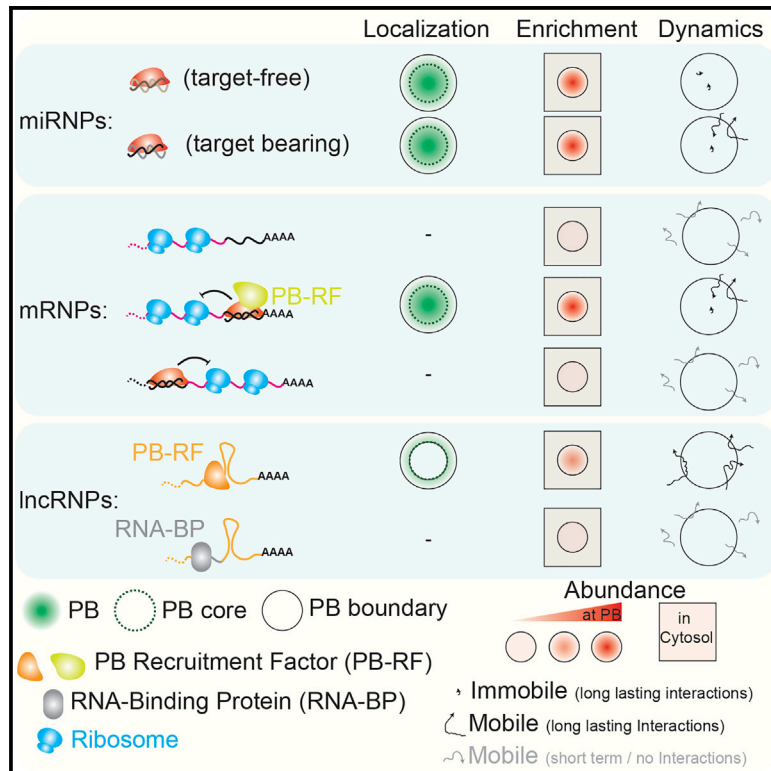


Molecular Cell

Dynamic Recruitment of Single RNAs to Processing Bodies Depends on RNA Functionality

Graphical Abstract



Authors

Sethuramasundaram Pitchiaya,
 Marcio D.A. Mourao,
 Ameya P. Jaliha, ...,
 Arul M. Chinnaiyan, Santiago Schnell,
 Nils G. Walter

Correspondence

sethu@umich.edu (S.P.),
 nwalter@umich.edu (N.G.W.)

In Brief

Single cellular RNAs stably or transiently associate with the core or periphery of processing bodies (PBs). The kinetics, localization patterns, and enrichment of RNAs at PBs depend on RNA type and function. Although PBs may not be designated sites of mRNA degradation, they contribute to miRNA surveillance.

Highlights

- RNAs exhibit diverse spatiotemporal localization patterns at PB core and periphery
- Extent of stable or transient RNA-PB interactions depends on RNA functionality
- Positioning of *cis*-regulatory miRNA target sites influences PB interaction kinetics
- PBs contribute to miRNA surveillance but less to mRNA decay



Dynamic Recruitment of Single RNAs to Processing Bodies Depends on RNA Functionality

Sethuramasundaram Pitchiaya,^{1,2,5,6,*} Marcio D.A. Mourao,^{3,4} Ameya P. Jaliha,¹ Lanbo Xiao,² Xia Jiang,² Arul M. Chinnaiyan,^{2,5,6,7} Santiago Schnell,³ and Nils G. Walter^{1,8,*}

¹Single Molecule Analysis Group, Department of Chemistry, University of Michigan, Ann Arbor, MI 48109-1055, USA

²Michigan Center for Translational Pathology, University of Michigan Medical School, Ann Arbor, MI 48109-1055, USA

³Department of Molecular and Integrative Physiology, University of Michigan Medical School, Ann Arbor, MI 48109-1055, USA

⁴Consulting for Statistics, Computing and Analytics Research, University of Michigan, Ann Arbor, MI 48109-1055, USA

⁵Department of Pathology, University of Michigan, Ann Arbor, MI 48109, USA

⁶Comprehensive Cancer Center, University of Michigan, Ann Arbor, MI 48109, USA

⁷Howard Hughes Medical Institute, University of Michigan, Ann Arbor, MI 48109, USA

⁸Lead Contact

*Correspondence: sethu@umich.edu (S.P.), nwalter@umich.edu (N.G.W.)

<https://doi.org/10.1016/j.molcel.2019.03.001>

SUMMARY

Cellular RNAs often colocalize with cytoplasmic, membrane-less ribonucleoprotein (RNP) granules enriched for RNA-processing enzymes, termed processing bodies (PBs). Here we track the dynamic localization of individual miRNAs, mRNAs, and long non-coding RNAs (lncRNAs) to PBs using intracellular single-molecule fluorescence microscopy. We find that unused miRNAs stably bind to PBs, whereas functional miRNAs, repressed mRNAs, and lncRNAs both transiently and stably localize within either the core or periphery of PBs, albeit to different extents. Consequently, translation potential and 3' versus 5' placement of miRNA target sites significantly affect the PB localization dynamics of mRNAs. Using computational modeling and supporting experimental approaches, we show that partitioning in the PB phase attenuates mRNA silencing, suggesting that physiological mRNA turnover occurs predominantly outside of PBs. Instead, our data support a PB role in sequestering unused miRNAs for surveillance and provide a framework for investigating the dynamic assembly of RNP granules by phase separation at single-molecule resolution.

INTRODUCTION

Sub-cellular membrane-free granules have emerged as critical components of normal biology and pathophysiology (Banani et al., 2017; Shin and Brangwynne, 2017) because of their key role in spatial regulation of gene expression (Martin and Ephrussi, 2009; Spector, 2006). Processing bodies (PBs) are one such class of ribonucleoprotein (RNP) granules that persist during cellular homeostasis and are enriched for RNA processing and degradation

enzymes (Eulalio et al., 2007a; Parker and Sheth, 2007). These granules are observed in almost all eukaryotes, ranging from yeast to mammals, and have been implicated in multiple biological processes, including oogenesis, progression through early development, and mediation of neuroplasticity (Buchan, 2014).

More specifically, mammalian PBs have been functionally associated with storage, translational repression, and/or degradation of mRNAs (Buchan, 2014; Hubstenberger et al., 2017; Liu et al., 2005; Schütz et al., 2017); as a result, PBs are predominantly composed of translationally repressed mRNAs, mRNA-regulating microRNAs (miRNAs), and, to a lesser extent, regulatory long non-coding RNAs (lncRNAs). Such a large RNP complex is hypothesized to assemble via RNA-dependent phase separation (Banani et al., 2017), wherein multiple translationally repressed RNPs are concentrated within dense foci through strong multivalent interactions, and individual or oligomeric RNPs loosely interact with these dense regions to create dynamic shells (Cougot et al., 2012; Van Treeck and Parker, 2018). Consequently, PBs, as whole granules, display a wide array of dynamic behaviors (Aizer et al., 2008), but the intra- and peri-granular RNP dynamics and RNP recruitment—processes that govern the maintenance, maturation, and putative gene-regulatory functions of PBs—are largely unknown. Although messenger ribonucleoprotein (mRNP)-PB colocalization and mRNA regulation have been shown to be tightly correlated (Buchan, 2014; Parker and Sheth, 2007), the question of whether mRNPs are degraded at microscopically visible and, thus, relatively large (>250 nm) PBs remains unresolved.

Here we dissect the fundamental principles governing the dynamic localization of functionally distinct classes of RNPs at phase-separated PBs and unravel the functional consequence of RNA-PB colocalization. To this end, we developed methodologies to simultaneously observe single RNA molecules (miRNAs, mRNAs, or lncRNAs) and individual PB foci in both living and fixed human cells. We demonstrate that the majority of miRNAs and repressed mRNAs are stably anchored within PBs, whereas translationally active mRNAs and lncRNAs associate with PBs only transiently, suggesting a strong correlation between PB



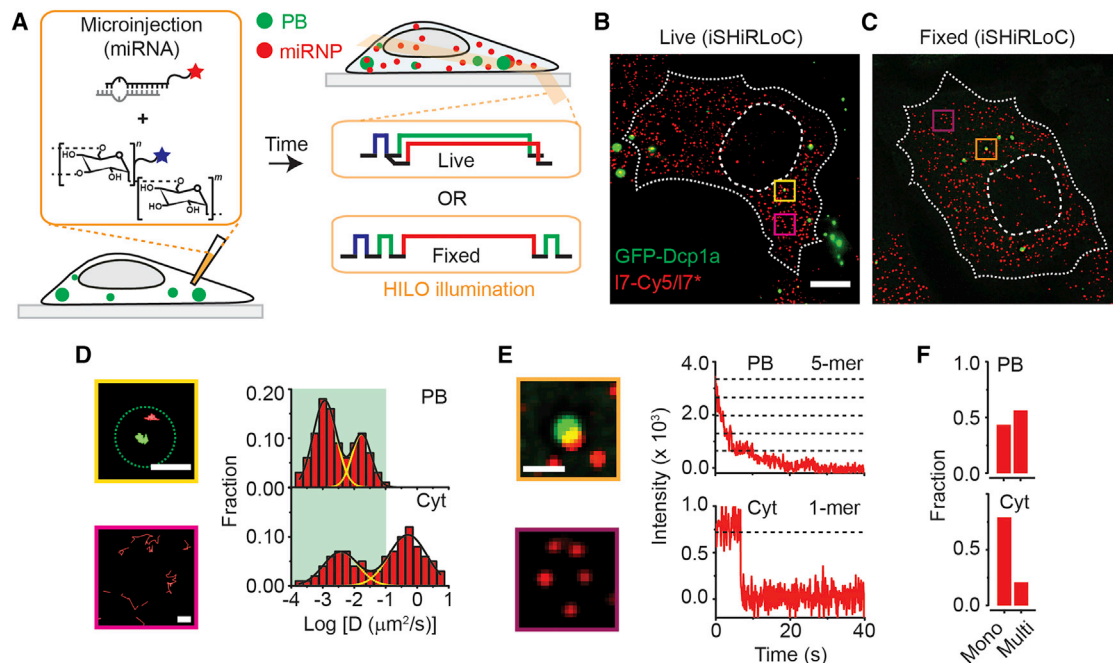


Figure 1. A Super-Resolution Imaging Tool for Probing RNA-Granule Dynamics and Stoichiometry

(A) Schematic of the iSHIRLoC assay for probing miRNA-PB dynamics and colocalization.

(B and C) Representative pseudocolored and contrast-adjusted images from live-cell imaging (B) and fixed-cell imaging (C) assays of UGD cells expressing GFP-labeled PBs (green) that were microinjected with I7-Cy5/I7* miRNA (red) and imaged 2 h after injection. Scale bar, 10 μ m.

(D) Representative single-particle trajectories of PBs (green) and I7-Cy5/I7* miRNA (red) from the yellow and magenta boxes in (B), representing diffusing miRNAs in PBs and in the cytoplasm (Cyt), respectively. Scale bar, 1 μ m. The dotted green circle represents the PB outline in the first frame of the video. Distribution of I7-Cy5/I7* miRNA diffusion constants in PB and Cyt are also depicted. The green area on the plot depicts the range of PB diffusion constants ($n = 3, 15$ cells).

(E) Magnified view of the orange and violet boxes in (C) from fixed UGD cells. Scale bar, 2 μ m. Stepwise photobleaching trajectories of PB- and Cyt-localized I7-Cy5/I7* are also shown.

(F) Distribution of I7-Cy5/I7* miRNA stoichiometry as monomeric (Mono, 1 photobleaching step) or multimeric (Multi, 2 or more photobleaching steps) complexes in PB and Cyt within fixed UGD cells ($n = 3, 15$ cells).

See also Figure S1.

localization and RNA class. Although miRNAs and mRNAs localized at the core or shells of PBs, lncRNAs were predominantly found at PB shells. Furthermore, we found that unused (target-less) miRNAs are enriched at PBs and that the 3' versus 5' terminal positioning of *cis*-regulatory miRNA response elements (MREs) dictates the PB localization patterns and dynamics of mRNAs. Finally, *in silico* modeling and experimental validation through hyperosmotic stress-induced phase separation suggest that the stochastic collision of mRNAs with freely diffusing, sub-microscopic PBs leads to more efficient mRNA regulation than their recruitment to microscopic PBs. Taken together, our observations reveal the nanoscale principles that govern the compositional complexity of mesoscale RNP granules and a novel suggested function for PBs in accumulating target-less miRNAs for miRNA surveillance.

RESULTS

Super-Resolved Single-Molecule Fluorescence Microscopy Probes RNA-PB Interactions

To dissect the localization dynamics of RNAs at and near PBs, we created a U2-OS cell line that stably expresses GFP-tagged Dcp1a, an mRNA-decapping co-activator and PB marker (Aizer

et al., 2008; Hubstenberger et al., 2017). We selected a clone (hereafter called UGD) with a similar number and composition (based on colocalization with other PB markers) of Dcp1a foci as endogenously found in U2-OS cells (Figures S1A–S1D). Next, mature regulatory miRNAs, whose size (~22 nt per strand) precludes endogenous labeling strategies (Pitchiaya et al., 2014), were chemically synthesized with a fluorescent Cy5 dye at the 3' end of one of their two complementary strands, typically the guide strand. Because transfection results in the sequestration of RNA within subcellular vesicles (Cardarelli et al., 2016), we chose to deliver these miRNAs via microinjection (Figures 1A–1C), which enables controlled delivery (Figures S1E–S1G) of physiologically relevant miRNA molecules per cell (~10,000–20,000 copies; i.e., one-tenth of the total number of miRNAs per cell) and defines a clear starting point for our assays by instantaneously exposing RNAs to the cellular milieu (Pitchiaya et al., 2012, 2013, 2017). We confirmed that fluorophore labeling and microinjection did not affect the gene-repressive function (Figures S1H–S1K) of let-7 miRNA (I7/I7* and I7-Cy5/I7*) (Pitchiaya et al., 2012), alter the sub-cellular abundance and behavior of PBs (Figures S1J and S1K), or induce stress granule (SG) formation (Figures S1L–S1O).

We then combined a super-registration fluorescence microscopy-based tool (Grünwald and Singer, 2010) that measures intermolecular distances of spectrally distinct fluorescent molecules with intracellular single-molecule, high-resolution localization and counting (iSHiLoC) (Pitchiaya et al., 2012, 2013, 2017). Consequently, we were able to visualize miRNA-PB interactions in living cells and precisely quantify miRNA stoichiometry within PBs in fixed cells (STAR Methods; Figures 1A–1C; Video S1). At a spatial accuracy of 30 nm and a temporal resolution of 50 ms, we can visualize large (>400 kDa) miRNPs, such as miRISC:miRNP complexes, in living cells and all miRNPs, irrespective of RNP size, in fixed cells (Figure S1P; Pitchiaya et al., 2012, 2013, 2017). Using this new tool, we found that the tumor suppressive let-7 miRNA (I7-Cy5/I7*) diffused ~100- to 1,000-fold slower at PBs compared with in the cytosol (Figure 1G), supporting the notion that miRNAs physically dock to form higher-order complexes at PBs, consistent with previous ensemble observations of miRNA accumulation at PBs (Liu et al., 2005; Pillai et al., 2005). However, we additionally observed that PB-localized miRNAs distributed between (at least) two populations of diffusion coefficients or molecular weights. Complementarily, fixed-cell analysis showed that cytoplasmic I7-Cy5/I7* miRNAs were predominantly monomeric; a significant minority of monomeric (~40%) and a predominant fraction of multimeric (~60%) RNA complexes (Figure 1H) were observed at PBs. Moreover, the PB dynamics and localization extents of I7-Cy5/I7* in GFP-Dcp1a-expressing HeLa cells were almost identical to those in UGD cells (Figures S1Q–S1R), underscoring the generality of our observations across cellular systems. Our data suggest that miRNPs of diverse sizes and, perhaps, composition localize to PBs via potentially distinct mechanisms, with the possibility to yield distinct regulatory outcomes.

miRNAs Stably or Transiently Localize at the Core or Periphery of PBs

We next sought to understand whether the observed diverse miRNP diffusion and assembly states at PBs are based on the type of miRNA-PB interaction. To this end, we first inspected individual trajectories of PB-localized I7-Cy5/I7* in live cells to discover diversities in the kinetics and modalities of miRNA-PB interactions. We identified five distinct types of RNA-PB interactions, each of which could be classified by a unique combination of diffusion coefficient (D), photobleaching-corrected dwell time (T), and percentage of an RNA track colocalizing with a PB (P) (Figures 2A and S2A; Video S2): (1) RNAs stably anchoring at PBs ($D = 0.0001\text{--}0.1\ \mu\text{m}^2/\text{s}$, $T \geq 15\ \text{s}$, $p = 100\%$; Video S2), (2) RNAs displaying significant dynamics within PBs ($D = 0.001\text{--}0.1\ \mu\text{m}^2/\text{s}$, $T \geq 15\ \text{s}$, $p = 100\%$; Video S2), (3) RNAs entering PBs from the cytosol ($D = 0.0001\text{--}0.01\ \mu\text{m}^2/\text{s}$, $T = 7.9 \pm 0.7\ \text{s}$, $p = 52\%\text{--}89\%$; Video S2), (4) RNAs transiently probing PBs ($D = 0.0001\text{--}1\ \mu\text{m}^2/\text{s}$, $T = 0.9 \pm 0.1\ \text{s}$, $p = 3\%\text{--}72\%$; Video S2), and (5) RNAs exiting a PB into the cytosol ($D = 0.0001\text{--}1\ \mu\text{m}^2/\text{s}$, $T = 0.8 \pm 0.1\ \text{s}$, $p = 7\%\text{--}83\%$; Video S2). The first three and latter two interaction types depict what we refer to as stable and transient RNA-PB localizations, respectively. These data suggest that the diffusion rates and dwell times of miRNPs define the type of interaction with PBs. Next we quantified the relative localization of PB-resident proteins or a few control proteins

with respect to GFP-Dcp1a (Figure S2B). Using this intra-granular localization atlas as a template, we spatially mapped the localization of miRNPs with reference to PB boundaries and found that miRNAs localized near the core or the periphery (or shell) of PBs in fixed cells (Figure 2B). We then performed ratiometric quantification of the core- or shell-localized immunofluorescence (IF) signal at PBs and the adjacent cytosol (Figure S2C), which yields similar information as the average percentage of IF signal within PBs per cell but also accounts for any heterogeneities between PBs within the same cell, and created a small compendium of proteins that were either enriched for (>1) or depleted (<1) of PBs (Figure S2C). Combining this new quantification tool with single-molecule counting, we discovered that miRNAs were either clustered (enriched within PBs compared with the adjacent cytosol) or dispersed at PBs (Figure 2C). As a control, we also probed dl7-Cy5/dl7*, a control DNA oligonucleotide of the same sequence as let-7 miRNA but incompetent for RNA silencing. In contrast to I7-Cy5/I7*, and as expected, we found that dl7-Cy5/dl7* neither localized to nor was enriched at (or near) PBs (Figure 2D). Taken together, these findings unravel a potentially tight relationship between miRNP composition and type of miRNP-PB interaction and the requirement for small double-stranded oligonucleotides to assemble into large RNPs to stably interact with PBs.

mRNA-Targeting and Target-Free miRNAs Are Both Enriched at PBs but Display Distinct PB Localization Dynamics

Based on our observations that a functionally repressive I7-Cy5/I7* miRNA dynamically localized to PBs via diverse modes (Figure 2), we hypothesized that the regulatory potential of miRNAs affects their PB localization. To test this hypothesis, we compared the PB localization of functional I7-Cy5/I7* with I7/I7*-Cy5, let-7 miRNA Cy5-labeled on the passenger instead of the guide strand, where the passenger strand has very few endogenous targets and is at least 8-fold less stable than the guide strand, and with ml7-Cy5/ml7*, a seed sequence-mutated let-7 miRNA variant that cannot bind endogenous let-7 targets and is at least 4-fold less stable than let-7 miRNA (Figure 3A; Pitchiaya et al., 2017). Strikingly, the fractional extent of PB localization and enrichment was significant and similar for I7-Cy5/I7*, I7/I7*-Cy5, and ml7-Cy5/ml7* (Figures 3B and 3C). Similar trends (Figures S3A–S3C) were observed for all other small double-stranded RNAs (dsRNAs)—namely, an oncogenic miRNA, miR-21 (m21-Cy5/m21*); an artificial miRNA, cxcr4 (cx-Cy5/cx*); and scrambled control dsRNA (Scr-Cy5/Scr*). Considering that each of these dsRNAs has distinct regulatory potential and intracellular stability (Pitchiaya et al., 2017), our data strongly suggest that miRNA functionality is not necessary for PB localization. However, ml7-Cy5/ml7*, I7/I7*-Cy5, cx-Cy5/cx*, and Scr-Cy5/Scr* rarely displayed any transient interactions (Figure 3D; Figure S3D) but, instead, exhibited monophasic dwell time distributions, residing in PBs for 15 s or longer (Figures 3D and S3), significantly different from the PB dynamics of I7-Cy5/I7* and m21-Cy5/m21*. These observations suggest that transient PB interactions of an miRNA are correlated with its ability to target mRNAs, whereas unused (target-less) miRNAs are more stably recruited to PBs. Further corroborating this notion,

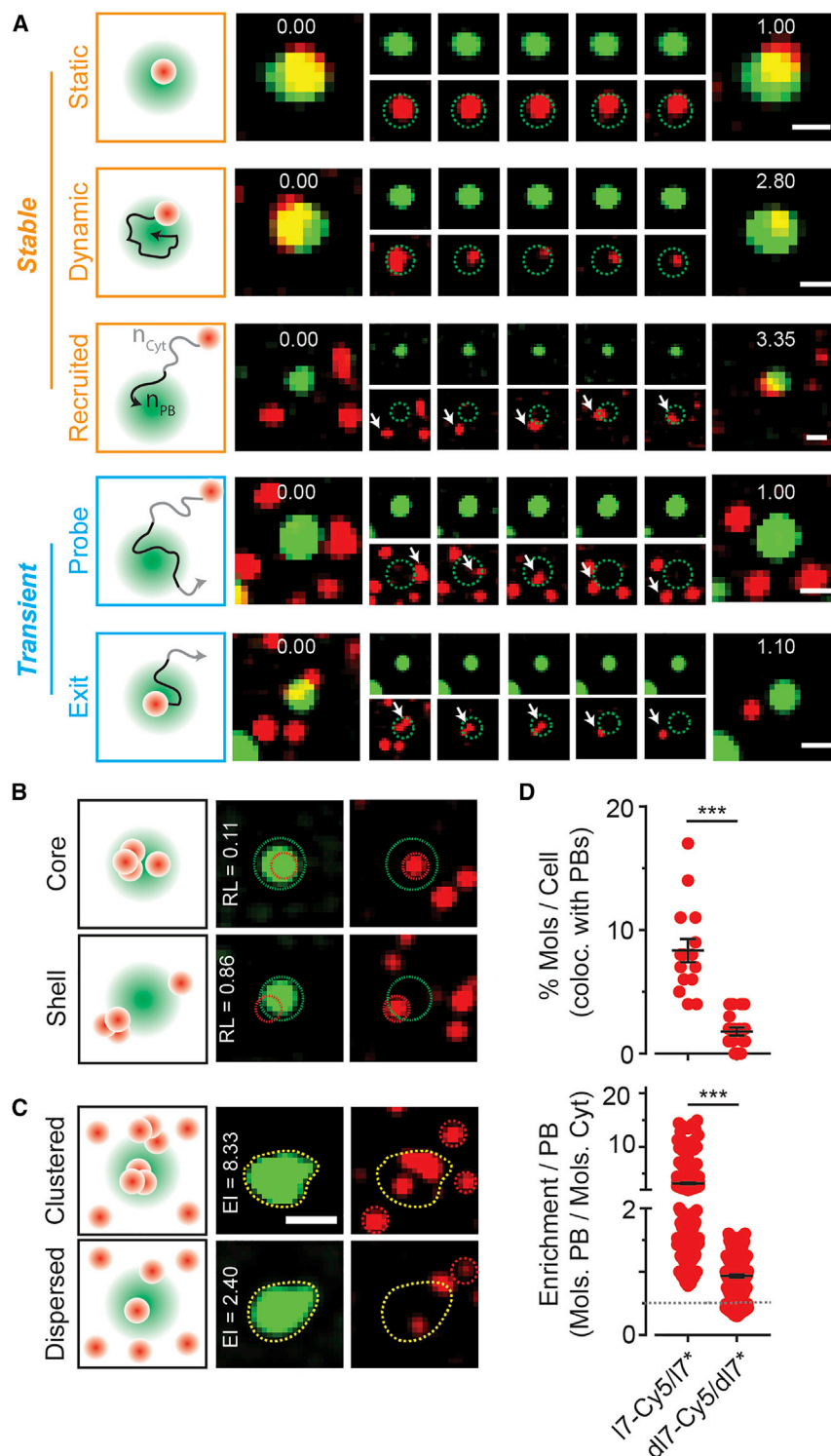


Figure 2. miRNAs Show Diverse Spatiotemporal Localization Patterns at the PB Core and Periphery

(A) Schematic and representative time-lapse images of PBs (green) and I7-Cy5/I7* miRNAs (red) in live UGD cells. Scale bar, 1 μ m. Embedded numbers in green or red overlay images (far left and far right) represent time in seconds. Dotted green circles in the red images have been included to aid in the identification of PB boundaries. White arrows point to individual RNA particles. Stable RNA-PB association patterns (static, dynamic, and recruited) are represented in orange, whereas transient ones (probe and escape) are represented in blue. n_{PB} , number of track localizations within PBs; n_{Cyt} , number of track localizations in the cytosol.

(B) Schematic and representative images of PBs (green) and I7-Cy5/I7* (red) representing the localization of miRNAs within shells or cores of PBs in fixed UGD cells. Dotted green and red circles represent boundaries of PBs and miRNAs, respectively. Relative localization values of I7-Cy5/I7* for these representative colocalizations are embedded in the green images.

(C) Schematic and representative images of PBs (green) and I7-Cy5/I7* (red) representing the enrichment of miRNAs in PBs within fixed UGD cells. Dotted yellow and red circles represent PB-miRNA colocalization and cytoplasmic miRNAs, respectively. Enrichment of I7-Cy5/I7* per PB (EI, enrichment index) for these representative colocalizations are embedded in the green images. Images are scaled as in (B).

(D) Scatterplot representing the percentage of RNA or DNA molecules that colocalize with PBs per fixed UGD cell (top). Each dot represents a cell. A scatterplot of enrichment of molecules per PB (bottom) is also shown. Each dot represents an individual PB in fixed UGD cells. $n = 3$, more than 15 cells, *** $p \leq 0.0001$ by two-tailed, unpaired Student's t test. The gray dotted line depicts an EI of one, which demarcates PB-enriched (>1) from PB-depleted (<1) factors.

See also Figure S2.

our results are consistent with PBs stably capturing target-less, non-coding miRNAs for surveillance and suggest that, instead, transient PB interactions are dominant for functional miRNAs engaging mRNA targets.

miRNA-Targeted mRNAs Localize to PBs Depending on 3' versus 5' Terminal Positioning of MREs

Next we probed whether miRNAs and their cognate mRNA targets display

we found that, upon co-microinjecting its cognate (RL-mI7-2x) mRNA, the mRNA-targeting mI7-Cy5/mI7* exhibited a substantial 5-fold increase in the fraction of transient interactions, resulting in a biphasic dwell time distribution with $T_{fast} = 0.7$ s and $T_{slow} = 13.2$ s (Figures 3E, 3F, S3C, and S3D). Taken together,

similar dynamics and localization patterns at PBs. mRNAs were endogenously expressed and tagged via a modified version of the widely used MS2-MCP labeling system (Fusco et al., 2003), wherein a total of up to $\sim 1,000$ Halo-MCP-bound MS2-RNA molecules were visualized per living cell

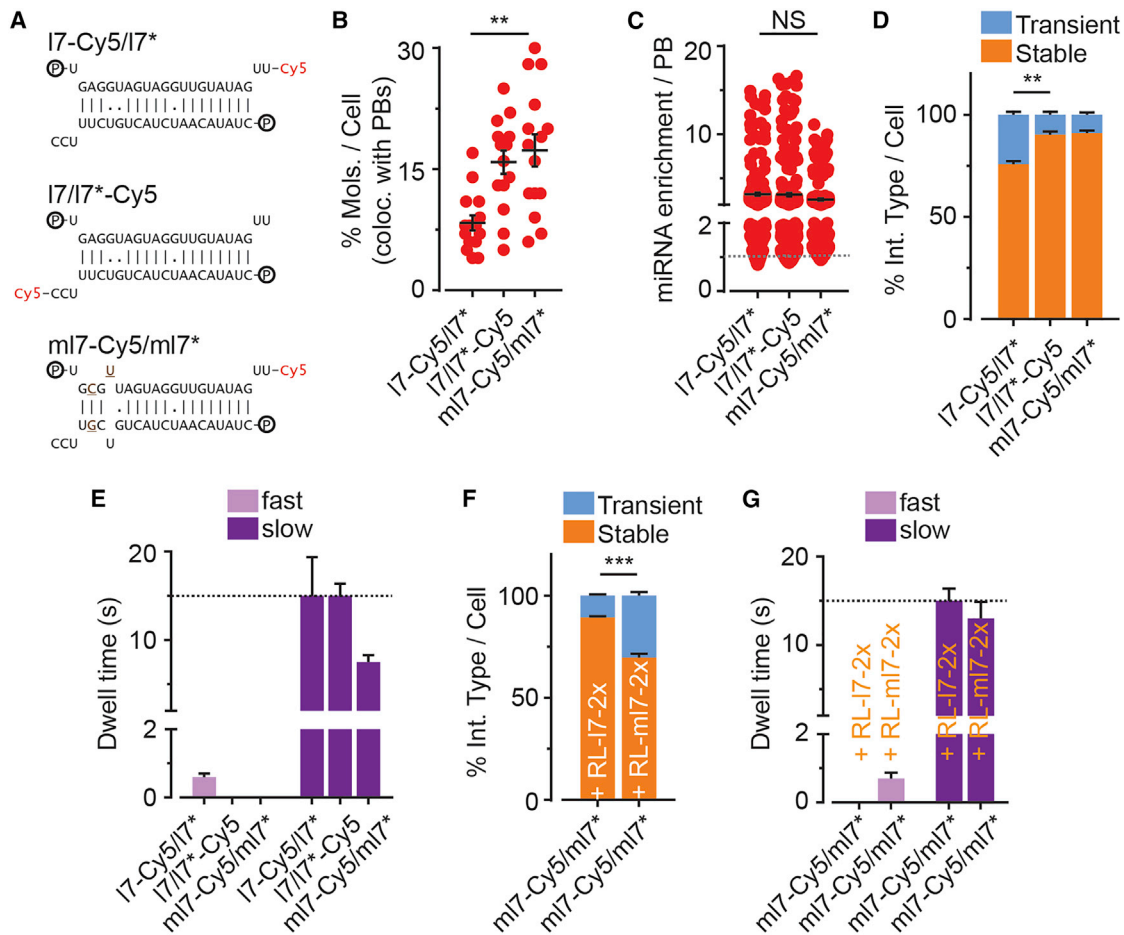


Figure 3. miRNA Functionality Influences miRNA-PB Interaction Kinetics

(A) Schematic of miRNAs used. P, lines, and dots represent 5' phosphate, Watson-Crick base-pairing, and wobble pairing, respectively. (B) Scatterplot representing the percentage of RNA or DNA molecules that colocalize with PBs per fixed UGD cell. Each dot represents a cell. (C) Scatterplot of EI for different constructs. Each dot represents an individual PB in fixed UGD cells. The gray dotted line depicts an EI of one, which demarcates PB-enriched (>1) from PB-depleted (<1) factors. (D) Relative distribution of stable and transient interactions per live UGD cell for different miRNAs. (E) Comparison of fast and slow miRNA-PB interaction kinetics in live UGD cells. (F) Relative distribution of stable and transient interactions per live UGD cell for mi7-Cy5/mi7* RNAs co-injected with a seed-mismatched (RL-I7-2x) or seed-matched (RL-mi7-2x) mRNA target. (G) Comparison of fast and slow mi7-Cy5/mi7*-PB interaction kinetics in the presence of a seed-mismatched (RL-I7-2x) or seed-matched (RL-mi7-2x) mRNA target in live UGD cells.

$n = 3$; 15 cells per sample; NS, not significant; ** $p \leq 0.001$ or *** $p \leq 0.0001$ by two-tailed, unpaired Student's t test. See also Figure S3.

upon covalently coupling the Halo tag with the cell-permeable fluorescent dye JF646 (Figures 4A and 4B; Video S3; Grimm et al., 2015). mRNAs in fixed cells were instead visualized by standard single-molecule fluorescence *in situ* hybridization (smFISH; Figures 4A and 4C; Raj et al., 2008). We created an MS2-MCP-tagged construct bearing the firefly luciferase (FL) coding sequence (CDS) and an artificial 3' UTR bearing six tandem MREs for the tumor-suppressive let-7 miRNA (I7-6x). Upon performing live- and fixed-cell imaging, respectively, we found that the mobility and assembly of FL-I7-6x-MS2 mRNA was similar to its cognate I7-Cy5/I7* miRNA (Figures 1 and 4A–4F), strongly supporting the notion that a miRISC-mRNP complex interacts with PBs. As a control, we created an MS2-tagged

FL gene with mi7-6x, a 3' UTR composed of six tandem mutant MREs, mi7/mi7*, that are not targeted by endogenous let-7 (Figure 4G). Considering that MRE-containing mRNAs are repressed, irrespective of whether the MREs are in the 3' or 5' UTR of the mRNA (Lytle et al., 2007), we created additional control constructs with either I7-6x or mi7-6x in the 5' UTR of the MS2-tagged FL gene, termed I7-6x-FL-MS2 and mi7-6x-FL-MS2, respectively (Figure 4G). As expected, ensemble activity assays showed that all MS2-tagged constructs were translated and regulated much like their untagged counterparts (Figures S4A and S4B). FL-mi7-6x-MS2 and mi7-6x-FL-MS2 were expressed to a much higher extent (Figure 4H) than the let-7-MRE containing FL-I7-6x-MS2 and I7-6x-FL-MS2, which

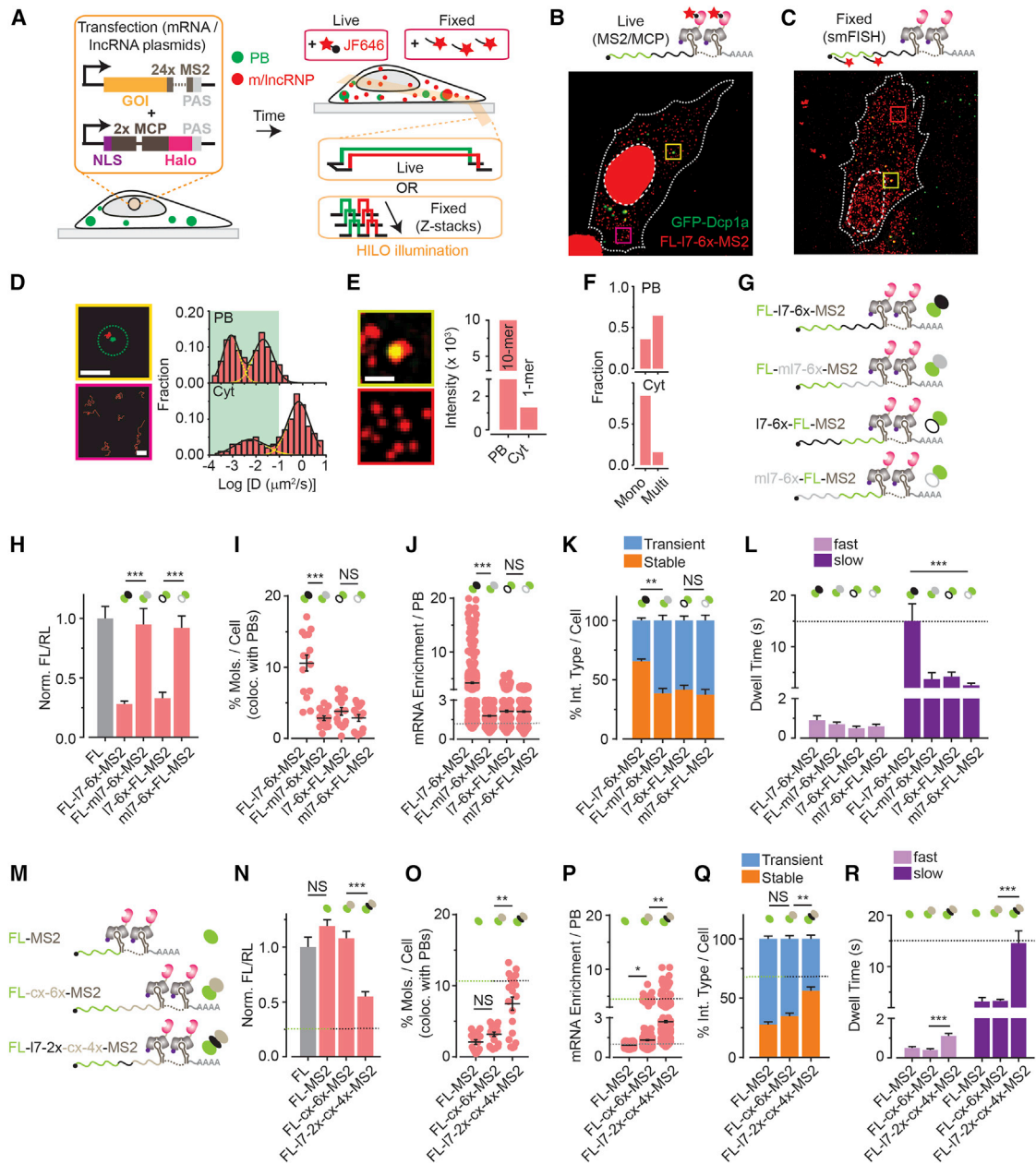


Figure 4. mRNAs Localize to PBs Depending on 3' versus 5' Terminal Positioning of MREs and Translation Potential

(A) Schematic of the assay for probing mRNA-PB dynamics and colocalizations.

(B and C) Representative pseudocolored and contrast-adjusted images from live-cell imaging (B) and fixed-cell imaging (C) assays of UGD cells expressing GFP-labeled PBs (green) and MCP-tagged FL-I7-6x-MS2 mRNAs (red). Scale bar, 10 μ m.

(D) Representative single-particle trajectories of PBs (green) and FL-I7-6x-MS2 mRNAs (red) from the yellow and magenta boxes in (B), representing diffusing mRNAs in PBs and in the Cyt, respectively. Scale bar, 1 μ m. The dotted green circle represents the PB outline in the first frame of the video. Distribution of FL-I7-6x-MS2 mRNA diffusion constants in PB and Cyt are also depicted. The green area on the plot depicts the range of PB diffusion constants (n = 3, 20 cells).

(E) Magnified view of the orange and violet boxes in (C) from fixed UGD cells. Scale bar, 2 μ m. Intensity measurements of PB- and Cyt-localized FL-I7-6x-MS2 mRNAs is also shown.

(F) Distribution of FL-I7-6x-MS2 mRNA stoichiometry as Mono (1 photobleaching step) or Multi (2 or more photobleaching steps) complexes in PB and Cyt within fixed UGD cells (n = 3, 20 cells).

(G and M) Schematic of different mRNA constructs with various 3' or 5' UTRs. Color-coded symbols for each transcript are shown and are used to depict these respective transcripts hereafter.

(legend continued on next page)

were both similarly repressed by let-7 miRNA (Figures 4H and S4C), thus corroborating prior reports that MREs embedded in either the 3' or 5' UTR are functional. However, the fractional extent of localization and enrichment of I7-6x-FL-MS2 at PBs was similar to that of the non-targeted FL-mI7-6x-MS2 and mI7-6x-FL-MS2 and significantly (at least 5-fold) lower than that of FL-I7-6x-MS2 (Figures 4I and 4J). Still, I7-6x-FL-MS2, FL-mI7-6x-MS2, and mI7-6x-FL-MS2, much like FL-I7-6x-MS2, interacted transiently with PBs and displayed biphasic interaction kinetics (Figures 4K, 4L, and S4D). Although the "fast" phase of I7-6x-FL-MS2, FL-mI7-6x-MS2, and mI7-6x-FL-MS2 (spanning ~0.5, 0.7, and 0.6 s, respectively) was similar to that of FL-I7-6x-MS2 (0.9 s), the "slow" phase of these constructs was ~3-fold faster than that of FL-I7-6x-MS2 (4.2, 3.7, and 2.5 s, respectively, compared with 15 s; Figure 4K), indicating a significant difference in behavior upon targeting the 3' versus 5' UTR. Similarly, a minority of I7-6x-FL-MS2, FL-mI7-6x-MS2, and mI7-6x-FL-MS2 particles did not photobleach and resided in PBs for the entire duration of acquisition (~15 s), with the number of such occurrences ~3-fold lower than for FL-I7-6x-MS2 (Figure S4E). Not only do these observations strongly support the notion that miRNAs and their cognate mRNA targets display generally similar PB localization kinetics and patterns, consistent with the hypothesis that they interact, but they uniquely demonstrate that 3' UTR versus 5' UTR positioning of MREs distinctly affects PB colocalization in that only 3' UTR targeting leads to the most stable PB interactions. We posit that distinct aspects of translation are blocked when miRNAs engage the 3' UTR versus 5' UTR, resulting in compositionally distinct mRNPs that differentially recruit them to PBs.

mRNA-PB Interactions Depend on Translation Potential

Given that translationally unrepressed mutant FL-mI7-6x-MS2 and translationally repressed FL-I7-6x-MS2 mRNAs displayed distinct PB dynamics and localization patterns (Figure 4), we hypothesized that the translation potential of an mRNA inversely correlates with PB localization. To test this hypothesis, we compared the PB localization dynamics of the let-7-regulated FL-I7-6x-MS2 mRNA (Figure 4) with those of FL-MS2 (lacking the regulatory 3' UTR), FL-I7-2x-cx-4x-MS2 (carrying a 3' UTR with two tandem MREs targetable by endogenous let-7 and four MREs for a non-endogenous cxcr4 miRNA), and FL-CX-6x-MS2 (carrying a 3' UTR with six tandem MREs for cxcr4 miRNA) (Figure 4M). Notably, the protein expression of FL-MS2 and FL-cx-6x-MS2 was significantly higher (~2.7 fold) than that of FL-I7-2x-cx-4x-MS2, which, in turn, was higher (~2.2-fold) than that of FL-I7-6x-MS2 (Figure 4N). Consistent

with our hypothesis, the fractional extent of localization and enrichment of FL-MS2 and FL-cx-6x-MS2 was significantly (at least 2.8-fold or 5-fold) lower than that of FL-I7-2x-cx-4x-MS2 or FL-I7-6x-MS2 (Figures 4G and 4H). Additionally, the interaction modalities and slow phase kinetics of FL-MS2 and FL-cx-6x-MS2 were distinct from those of FL-I7-2x-cx-4x-MS2 and FL-I7-6x-MS2, with the former set of constructs displaying at least ~2.5-fold more transient interactions and ~3-fold shorter dwell times at PBs (Figures 4I and 4J) compared with the latter set. A significant minority of FL-MS2 and FL-cx-6x-MS2 particles resided in PBs for the entire duration of acquisition (~15 s), potentially representing mRNAs that are currently translation-inactive, but the number of such occurrences was ~2.9-fold and ~4.5-fold lower than for FL-I7-2x-CX-4x-MS2 and FL-I7-6x-MS2 (Figure S4F), respectively. These observations strongly support the notion that actively translating mRNAs rarely localize to PBs and, conversely, that the propensity for PB localization increases with the extent of mRNA repression.

miRNA-Targeted mRNA Turnover Predominantly Occurs outside of PBs

We found that almost all visible PBs colocalize with miRNA or mRNA molecules, irrespective of relative RNA enrichment (Figures 2, 3, 4, and 5A) and that a single PB associates with at least 3 labeled RNA molecules within our timeframe of imaging (Figure 5B). Considering this frequent encounter of miRNA or mRNAs and PBs, that miRNA-mediated translational repression would eventually lead to RNA decay (Djuranovic et al., 2012), and that PBs are enriched for mRNA degradation enzymes (Hubstenberger et al., 2017; Parker and Sheth, 2007), we sought to test whether PBs are designated sites of RNA decay responsible for the bulk of cellular mRNA turnover. Although fluorescence microscopy can visualize large PBs (>50 nm), it does not capture smaller functional complexes of RNA decay enzymes. We therefore kinetically computationally modeled (Mourão et al., 2014) the mRNA degradation activity of microscopically visible and invisible PBs (Figure 5C). We specifically tested miRNA-mediated mRNA decay, largely because of its cellular prevalence and prior reports of miRNA-programmed mRNA localization to PBs; however, our method is extendable to other decay processes. We devised a basic set of reactions, each with predefined rates, whereby the interaction of miRISC with mRNPs activates PB-mediated mRNA degradation. Upon computing the copy number of each of these molecular species as they diffused across the lattice through time, we found that mRNA degradation was most efficient when there was a large number of small, mobile PBs (Figure 5C). That is, although degradation is possible

(H and N) Luciferase reporter assays represented as the ratio of luminescence from a firefly luciferase (FL) reporter gene and a *Renilla* luciferase (RL) normalization gene in UGD cells. Data were normalized to the FL sample. Mean and SEM are represented ($n = 12$ replicates, *** $p < 0.0001$ based on two-tailed, unpaired Student's t test).

(I and O) Scatterplot representing the percentage of mRNA molecules that colocalize with PBs per fixed UGD cell. Each dot represents a fixed UGD cell.

(J and P) Scatterplot of EI for different mRNA constructs. Each dot represents a PB in fixed UGD cells. The gray dotted lines represent an EI of one, which demarcates PB-enriched (>1) from PB-depleted (<1) factors.

(K and Q) Relative distribution of stable and transient interactions per live UGD cell for different mRNAs.

(L and R) Comparison of fast and slow mRNA-PB interaction kinetics in live UGD cells. Black lines indicate the acquisition window (15 s). Green-black lines indicate the mean magnitude of FL-I7-6x-MS2 for the respective observable.

$n = 3$; 15 or more cells per sample; * $p \leq 0.01$, ** $p \leq 0.001$, or *** $p \leq 0.0001$ by two-tailed, unpaired Student's t test. See also Figure S4.

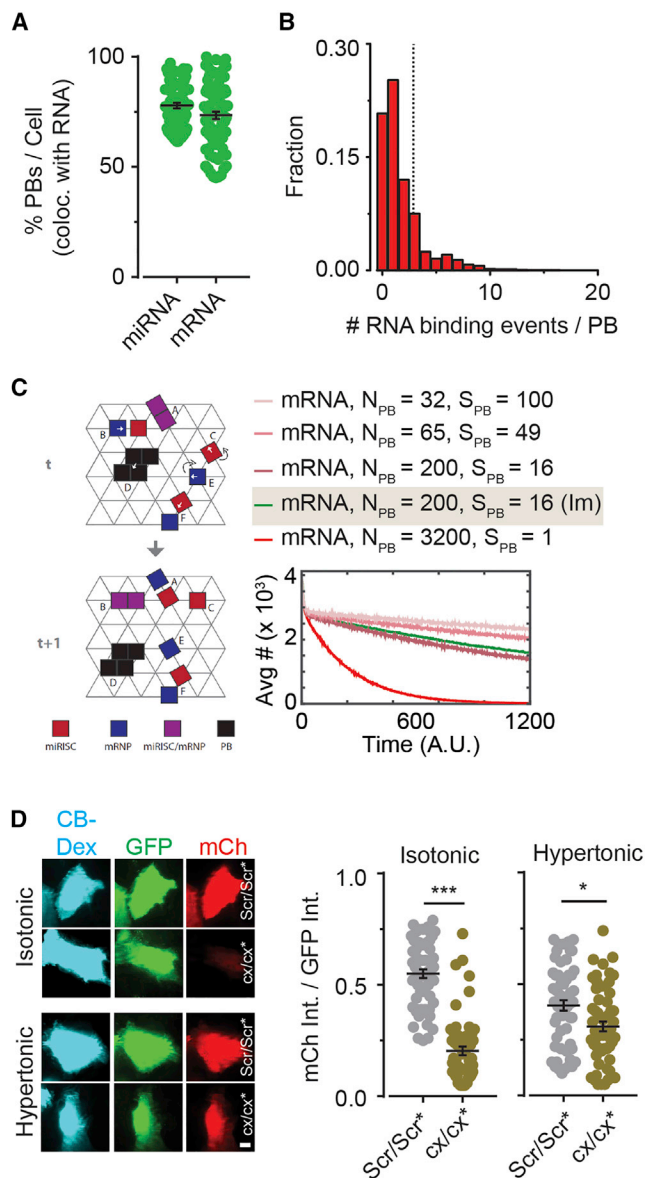


Figure 5. The Majority of Microscopically Visible PBs Associate with mRNAs, but mRNAs Are More Effectively Degraded with a Larger Number of Smaller, Microscopically Invisible PBs

(A) Scatterplot representing the percentage of PBs that colocalize with RNAs per fixed UGD cell ($n = 3, 15$ or more cells per sample).

(B) Frequency distribution of the number of times an individual PB encounters an RNA in live UGD cells ($n = 3, 155$ cells, 2,102 PBs). The dotted line represents the average number of RNA encounters per PB after correcting for photobleaching.

(C) Schematic (left) of *in silico* kinetic modeling of RNA-PB interactions and RNA decay. Changes in the abundance of mRNA over the timescale of the simulation is also depicted (right). Im (highlighted text) represents simulations in which PBs were immobile, whereas PBs were mobile under all other conditions.

(D) Experimental validation of simulations using a microinjection-based miRNA activity assay. Left: representative images of U2-OS cells treated with isotonic or hypertonic (300 mM Na⁺) medium and co-injected with cascade blue (CB)-Dextran, GFP mRNA, mCh mRNA with MREs for cx/cx* (cx/cx*) miRNA, and either a scrambled control siRNA (Scr/Scr*) or cx/cx*. Images were

within large, microscopically visible PBs, the process is most efficient when degradation factors, perhaps individual molecules, are unconstrained in the cell, presenting a large surface area for capturing repressed mRNAs.

To test our *in silico* predictions experimentally, we resorted to modulating PB number and size via hyperosmotic stress, a method that has been proven to increase PB numbers in yeast (Huch and Nissan, 2017). We confirmed that hyperosmotic treatment of UGD cells results in a high number of immobile GFP-Dcp1a foci (Figures S5A–S5D), which form because of local association of previously mobile, microscopically unresolved GFP-Dcp1a proteins, an aspect that is efficiently recapitulated by our *in silico* kinetic modeling approach (Figure 5C, Im). Microinjection-based miRNA activity assays (Figure S1E) in U2-OS cells suggested that, as predicted, miRNA-mediated gene repression is alleviated when PBs are aggregated when subjecting cells to hyperosmotic stress (Figure 5D). Taken together, our data predict that mRNA degradation is primarily mediated by degradation enzymes rendered more efficient by freely diffusing in the cytosol, relegating PBs to degrading only a small fraction of repressed mRNAs.

lncRNA-PB Interactions Are Distinct from Those of Regulatory miRNAs and Repressed mRNAs

Having discovered the importance of translation versus translational repression in mRNA-PB colocalization behavior, we hypothesized that lncRNAs that sparsely interact with the translational machinery must localize to PBs via mechanisms distinct from those involving miRNAs and mRNAs. To address this hypothesis, we chose as model the nucleocytoplasmic lncRNA THOR (Figure 6A), which binds PB-enriched IGF2BP1 protein (Hubstenberger et al., 2017). We confirmed that THOR-MS2 still mediates the oncogenic phenotype of the unmodified lncRNA (Hosono et al., 2017), as evident by its promotion of cell growth and stimulation of oncogene expression (Figures S6A–S6C). We then performed live-cell imaging assays (Video S4) and found that THOR-MS2 molecules, on an average, diffused faster than the miRNAs or mRNAs we imaged but distributed between at least two populations of diffusion constants at PBs, much like the other RNAs (Figure S6D). Fixed-cell imaging showed that the stoichiometry of THOR at PBs was marginally higher than that found in the cytosol (Figures 6B and S6E). Although the fractional extent of RNA-PB colocalization did not significantly differ between mRNAs on one hand and lncRNAs on the other (Figures 6C and 6D), we found significant differences in the localization patterns and interaction kinetics between miRNA or mRNAs and THOR-MS2 lncRNAs (Figure 6). In particular, THOR-MS2 frequently localized to the shell of PBs, whereas I7-Cy5/I7* miRNA or FL-I7-6x-MS2 mRNA, ~2.5- to 5-fold more PB-enriched than THOR-MS2, predominantly localized near PB cores (Figure 6E). We also observed that a THOR version lacking IGF2BP1 binding sites (THOR-Δbs-MS2) only rarely localized

acquired 4 h after injection. Right: scatterplot representing the ratio of mCh:GFP intensity under various injection and treatment conditions. Each dot represents a U2-OS cell ($n = 3, 60$ cells for each sample). See also Figure S5.

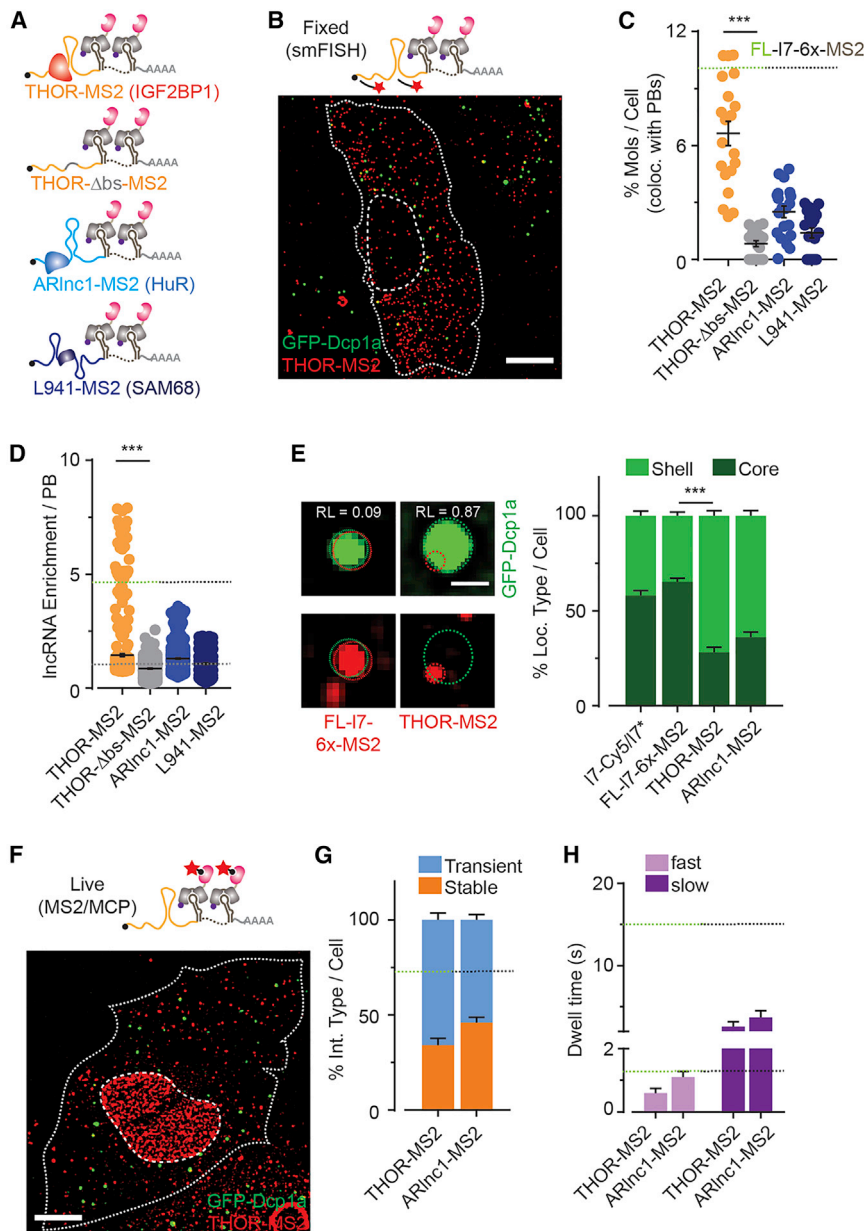


Figure 6. IncRNAs Transiently Interact with PB Peripheries

(A) Schematic of different IncRNA constructs bound by their respective interacting protein partners. (B) Representative pseudocolored and contrast-adjusted images of fixed a UGD cell expressing GFP-Dcp1a (green) and stained for THOR-MS2 via smFISH (red). Dotted line, cell and nuclear outline. Scale bar, 10 μ m.

(C) Scatterplot representing the percentage of IncRNA molecules per cell that colocalize with PBs. Each dot represents a cell.

(D) Scatterplot for the enrichment of IncRNAs at PBs. Each dot represents a PB. The gray dotted line indicates an EI of one, which demarcates PB-enriched (>1) from PB-depleted (<1) factors.

(E) Representative pseudocolored and contrast-adjusted regions of fixed UGD cells with GFP-Dcp1a (green), stained for FL-I7-6x-MS2 mRNA or THOR-MS2 IncRNA via smFISH (red). Green and red dotted circles represent boundaries of PBs and THOR-MS2, respectively. Scale bar, 2 μ m. The relative localization value is represented in the image. PB shell versus PB core localization distribution is also shown.

(F) Representative pseudocolored and contrast-adjusted images of live UGD cells expressing GFP-Dcp1a (green) and THOR-MS2 (red). Dotted line, cell and nuclear outline. Scale bar, 10 μ m.

(G) Relative distribution of stable and transient interactions per live UGD cell.

(H) Comparison of fast and slow interaction kinetics in live UGD cells. The green-black line depicts the mean magnitude of FL-I7-6x-MS2 for the respective observable.

$n = 3$; 15 or more cells per sample; * $p \leq 0.01$, ** $p \leq 0.001$, or *** $p \leq 0.0001$ by two-tailed, unpaired Student's t test. See also Figure S6.

to or interacted with PBs (Figures 6C and 6D), indicating that THOR-PB interactions are mediated by IGF2BP1. Moreover, THOR-MS2 displayed ~ 2 - to 3-fold more transient PB interactions than FL-I7-6x-MS2 mRNA (Figures 6F and 6G). Although the dwell time distributions were bi-phasic for both (Figures S5C and S6F), I7-Cy5/I7* miRNA and FL-I7-6x-MS2 mRNA ($T_{\text{fast}} = 0.6$ s and $T_{\text{slow}} \geq 15$ s) resided at PBs for a significantly longer time than THOR-MS2 ($T_{\text{fast}} = 0.6$ s and $T_{\text{slow}} = 2.9$ s; Figures 6B and S6B). We further found that the oncogenic lncRNA ARlnc1 (Zhang et al., 2018), known to bind PB-enriched HuR (Hubstenberger et al., 2017), displayed similar PB localization kinetics and patterns as THOR (Figures 6 and S6F), whereas oncogenic LINC00941 (L941) (Shukla et al., 2016), an lncRNA that

lacks consensus binding motifs for PB-enriched proteins (Hubstenberger et al., 2017), only rarely localized to PBs and displayed monophasic interaction kinetics, much like THOR- Δ bs-MS2 (Figures 6 and S6F). Together, these data support our hypothesis that regulatory miRNAs and miRNA-regulated mRNAs are stably captured by PBs; in contrast, regulatory, non-translating lncRNAs that bind PB-localizing protein factors only transiently associate with PBs. These specific but transient lncRNA-PB interactions are often missed in ensemble assays that largely rely on the enrichment of stable, high-affinity interactions, likely leading to the relative dearth of lncRNAs observed in the transcriptome of PB cores (Hubstenberger et al., 2017).

DISCUSSION

Previous reports have provided exquisite static snapshots of RNA and protein colocalization with PBs (Cougot et al., 2012; Horvathova et al., 2017; Kedersha and Anderson, 2007; Liu

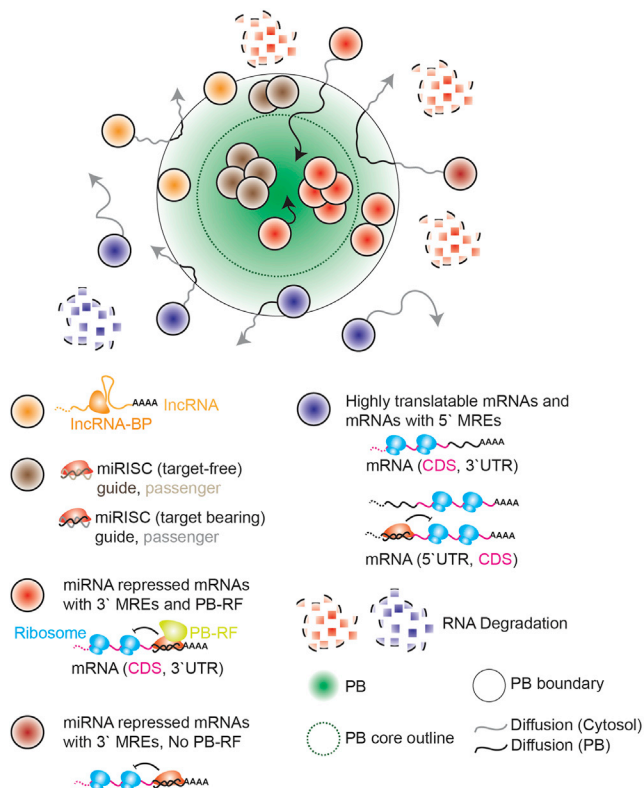


Figure 7. Resulting Model for the Dynamic Recruitment of Specific RNAs to PBs

RNAs dynamically associate with the PB core or shell based on functionality. Target-free miRNAs, mRNA-targeting miRNAs, and miRNA-targeted mRNAs with 3' UTR MREs are stably enriched within either cores or shells of PBs. The presence of a PB recruitment factor (PB-RF) may influence the dynamics and enrichment extent of miRNA-targeted mRNAs at PBs. IncRNAs transiently but specifically associate with PB shells when the IncRNA binding protein (IncRNA-BP) is a PB-enriched factor or a PB-RF. Other IncRNAs, translating mRNAs, and miRNA-targeted mRNAs with 5' UTR MREs transiently associate with PB shells or are excluded from PBs. The majority of nuclease-mediated RNA degradation occurs outside of PBs.

et al., 2005) but could not assess the dynamics of the underlying recruitment processes. Others have provided valuable information regarding the dynamics of PB movement and the bulk exchange of proteins or mRNAs between PBs and the cytosol but could not extract mechanistic information about the recruitment of biomolecules to PBs (Aizer et al., 2008, 2014; Kedersha et al., 2008; Leung et al., 2006). Using single-molecule live-cell imaging, here we uniquely demonstrate that miRNAs, mRNAs, and IncRNAs dynamically localize to PB either stably or transiently (Figures 1 and 2). Having dissected the molecular anatomy of PBs (Figure S2), we find that stable anchoring at PBs is concordant with snapshots that visually portray RNA accumulation within PB “cores,” whereas more mobile localizations and transient interactions are more likely to depict the localization of RNAs in PB “shells.” In agreement with our data on miRNA-, mRNA-, or IncRNA-PB interactions during cellular homeostasis, recent reports (Moon et al., 2019; Wilbertz et al., 2019) have complementarily shown that mRNAs associate both stably and

transiently with both SGs and PBs during the integrated stress response. The dwell times annotated as stable (~250 s) or transient (~10 s) in these reports are akin to particles in our datasets that dwell at PBs for the entire duration of acquisition (>15 s) and for ~3–5 s, respectively. We have found an additional, highly dynamic interaction mode that lasts ~1 s, which potentially represents a relatively rapid PB-probing step. Based on the dwell times of THOR-Δbs-MS2 and L941-MS2 (~0.1–0.3 s; Figure S6F; Table S2), which seldom localize to PBs, it is unlikely that the dynamic interaction mode (~1 s) is an artifact of coincidental interaction or co-localization of RNAs with PBs. Upon RNP remodeling, these rapid encounters may transition into longer spans of granule probing or stable docking of RNAs to granules.

Elucidation of the PB core transcriptome (Hubstenberger et al., 2017) has suggested that certain miRNAs, IncRNAs, and repressed mRNAs are enriched in PBs, but it is unclear whether the principles governing PB enrichment for these major classes of transcripts are similar or different. Strikingly, we found that miRNAs, mRNAs, and IncRNAs have distinct PB localization signatures that appear to be correlated with the distinct functionalities of these transcripts and the diversity in the types of RNPs they form (Figure 3). Based on our data, we propose a model that assigns PB localization patterns to specific RNA forms and functionalities (Figure 7). Stably anchored and PB-enriched miRNAs are predominantly dysfunctional; they do not have many mRNA targets and localize to PBs in their unbound or miRISC-bound (single-stranded or double-stranded) forms (Figure 4). Functional miRNAs, more likely to reside in RISC-mRNA complexes, display this behavior only in their minority and, when anchored, preferably localize within PB cores. These data are consistent with prior reports that both strands of both target-less and target-containing siRNAs localize to PBs (Jaky-miw et al., 2005). We posit that, in contrast, transient associations at PB peripheries represent miRISC-mRNA complexes that have not yet bound an important recruiting protein, such as GW182 or LAMP1 (Moon et al., 2019; Wilbertz et al., 2019), that is required for PB association. Conversely, highly translatable mRNAs that are not associated with miRNAs, although transiently associating peripherally, are not enriched at PBs. Based on recent reports (Moon et al., 2019; Wilbertz et al., 2019) and our data (Figures 2 and 3), we predict that non-translating mRNAs and translationally repressed mRNAs bearing MREs in their 3' UTR stably associate with PB cores, whereas only the latter are enriched at PBs. Furthermore, we find that miRNA-repressed mRNAs with MREs in the 5' UTR (Figures S5A and S5B) are not enriched at and only transiently associate with PBs, probably also because of the lack of a PB recruitment factor bound to these RNPs (Figure 5). Prior reports have demonstrated that MREs in the 5' UTR cause translational repression downstream of translation initiation sites (Lytle et al., 2007), potentially resulting in polysome-bound non-translating mRNAs, which consequently cannot enter ribosome-excluded PB cores (Parker and Sheth, 2007). In contrast, MREs in the 3' UTR typically result in inhibition of translation initiation, leading to non-translating mRNAs that are also free of ribosomes, which can then enter PB cores. Taken together, our data suggest that different modes of miRNA-mediated mRNA repression favor different types of PB localization.

THOR, ARlnc1, and LINC00941 are recently discovered oncogenic lncRNAs with distinct protein interactomes and functions. First, THOR is a highly conserved testis-specific lncRNA that is upregulated in a broad range of human cancers and has been found to work in concert with IGF2BP1 (Hosono et al., 2017), a PB-enriched protein (Hubstenberger et al., 2017) that stabilizes transcripts via CRD (coding region instability determinant)-mediated mRNA stabilization (Weidensdorfer et al., 2009). Second, ARlnc1 is a lineage-specific lncRNA that collaborates with the PB-enriched protein HuR to enhance the stability of transcripts bound via an RNA-RNA interaction (Zhang et al., 2018). Third, L941 is an lncRNA that is highly expressed in lung cancer (Shukla et al., 2016) and does not have consensus sequences for binding PB-resident proteins (data not shown). Based on our data, we propose that THOR, ARlnc1, and LINC00941 all assemble into slowly diffusing ($D = 0.0001\text{--}0.1 \mu\text{m}^2/\text{s}$; Figure S6D) RNPs that, we posit, correlate with their functions (Hosono et al., 2017). The frequent, transient associations of THOR and ARlnc1 with PBs may be linked to the regulatory role of these lncRNAs; one can envision (1) the lncRNAs depositing regulated mRNAs for storage at PBs or (2) the lncRNAs instead selecting PB-stored mRNAs for reintroduction into the translating cytoplasmic pool. Of note, we rarely observed any stable anchoring or significant enrichment of THOR, ARlnc1, or LINC00941 at PBs, which suggests that the mere inability of an RNA to be translated is not a sole prerequisite for stable PB association and enrichment. Moreover, the mere ability of THOR and ARlnc1 to bind RNA-stabilizing proteins (IGF2BP1 and HuR, respectively) may preclude stable, long-lasting interactions with PBs that are enriched for RNA-destabilizing factors. However, the relative contribution of stabilizing or destabilizing RBPs (RNA binding proteins) on PB recruitment of mRNAs is yet to be determined and will clearly identify the molecular driving forces of RNP recruitment into phase-separated granules and their subsequent regulation at these sites. Finally, our data also support the notion that ncRNA-PB interactions are dependent on the size, as reported for SGs (Khong et al., 2017), and class of the regulatory ncRNA (Figure 6).

More broadly, our molecular observations of colocalization of varying dynamics are consistent with phase transition principles that have recently been recognized to govern the assembly of large membrane-free granules (Protter and Parker, 2016; Shin and Brangwynne, 2017). Static, core-localized, and enriched RNPs may serve as nucleating factors for large PBs, whereas dynamic, shell-localized, and dispersed colocalization may occur when the interfaces of the RNP, PB, and surrounding cytoplasm are similar, as in a Neumann's triangle, observed in Cajal bodies attached to B-snurposomes (Shin and Brangwynne, 2017). Transient colocalizations may represent cases where the smaller RNP and PB come in close proximity, but the interfacial surface tension is too high for the two to fuse, presumably because of the absence of an appropriate PB recruitment factor on the RNP.

Although there is general agreement on the phase separation assembly principles of PBs and other RNA granules, the functions of these granules are still a topic of intense debate. Some reports have suggested that PBs may have stress-dependent RNA decay or storage roles (Aizer et al., 2014), whereas others have suggested that PBs are sites of RNA storage but not decay

(Eulalio et al., 2007b; Horvathova et al., 2017; Stalder and Mühlemann, 2009; Tutucci et al., 2018). Notably, all previous studies have examined only microscopically visible PBs. Our computational simulations, which considered PBs both large and small, together with subsequent experiments using hyperosmotic stress to induce PB aggregation, suggest that microscopically visible PBs cannot account for the bulk of cellular mRNA decay (Figure 6). Our data instead suggest that fundamental principles of physical chemistry hold true for mRNA regulation processes within the complex cellular environment, in that the entropic gain from the larger degree of freedom and surface area of freely diffusing decay components dominates, an aspect that warrants additional lines of investigation. In addition to storing repressed mRNAs, our work unveils an additional house-keeping role for PBs in storing or possibly degrading unused miRNAs for their surveillance. Super-resolved fluorescence microscopy is a powerful approach for mechanistically probing the dynamic assembly of RNP granules by phase separation at single-molecule resolution.

STAR★METHODS

Detailed methods are provided in the online version of this paper and include the following:

- KEY RESOURCES TABLE
- CONTACT FOR REAGENT AND RESOURCE SHARING
- EXPERIMENTAL MODEL AND SUBJECT DETAILS
 - Cell lines
- METHOD DETAILS
 - DNA, RNA and LNA oligonucleotides
 - Plasmids
 - mRNA synthesis
 - Luciferase reporter assays
 - RT-qPCR
 - Cell growth assays
 - Microinjection
 - Single-molecule fluorescence *in situ* hybridization
 - Immunofluorescence
 - Microscopy
 - Image analysis
 - *In silico* kinetic modeling
- QUANTIFICATION AND STATISTICAL ANALYSIS
- DATA AND SOFTWARE AVAILABILITY

SUPPLEMENTAL INFORMATION

Supplemental Information can be found online at <https://doi.org/10.1016/j.molcel.2019.03.001>.

ACKNOWLEDGMENTS

We thank T.C. Custer and M. Denies for technical assistance. We thank N. Kersha, D. Bartel, and R. Singer for generous gifts of plasmids containing GFP-Dcp1a, the 3' UTR of HMGA2, and the MS2 system of plasmids, respectively. We thank L. Lavis for providing the JF646 dye. We thank V. Krishnan for input on the manuscript. This work was supported by NIH grant R01 GM081025 and a University of Michigan Comprehensive Cancer Center/Bioinformatics Institute research grant (to N.G.W.). A.J. is supported by NIH cellular and molecular biology training grant T32-GM007315. A.M.C. is supported by the Prostate

Cancer Foundation and the Howard Hughes Medical Institute and is an American Cancer Society research professor. S.P. was supported by AACR-Bayer prostate cancer research fellowship 16-40-44-PITC. L.X. was supported by Department of Defense postdoctoral fellowship W81XWH-16-1-0195. We also acknowledge NSF MRI-ID grant DBI-0959823 (to N.G.W.) for seeding the Single Molecule Analysis in Real-Time (SMART) Center, whose Single Particle Tracker TIRFM equipment was used for much of this study.

AUTHOR CONTRIBUTIONS

S.P. designed and performed all assays. M.D.A.M. and S.S. performed the kinetic modeling. A.P.J. assisted with immunofluorescence assays. L.X. and X.J. created and validated mRNA and lncRNA constructs. S.P., S.S., A.M.C., and N.G.W. conceived the study, and all authors wrote the manuscript together.

DECLARATION OF INTERESTS

The authors declare no competing interests.

Received: July 20, 2018

Revised: December 21, 2018

Accepted: February 27, 2019

Published: April 2, 2019

REFERENCES

- Aizer, A., Brody, Y., Ler, L.W., Sonenberg, N., Singer, R.H., and Shav-Tal, Y. (2008). The dynamics of mammalian P body transport, assembly, and disassembly in vivo. *Mol. Biol. Cell* 19, 4154–4166.
- Aizer, A., Kalo, A., Kafri, P., Shraga, A., Ben-Yishay, R., Jacob, A., Kinor, N., and Shav-Tal, Y. (2014). Quantifying mRNA targeting to P-bodies in living human cells reveals their dual role in mRNA decay and storage. *J. Cell Sci.* 127, 4443–4456.
- Banani, S.F., Lee, H.O., Hyman, A.A., and Rosen, M.K. (2017). Biomolecular condensates: organizers of cellular biochemistry. *Nat. Rev. Mol. Cell Biol.* 18, 285–298.
- Buchan, J.R. (2014). mRNP granules. Assembly, function, and connections with disease. *RNA Biol.* 11, 1019–1030.
- Cardarelli, F., Digiaco, L., Marchini, C., Amici, A., Salomone, F., Fiume, G., Rossetta, A., Gratton, E., Pozzi, D., and Caracciolo, G. (2016). The intracellular trafficking mechanism of Lipofectamine-based transfection reagents and its implication for gene delivery. *Sci. Rep.* 6, 25879.
- Churchman, L.S., Oken, Z., Rock, R.S., Dawson, J.F., and Spudich, J.A. (2005). Single molecule high-resolution colocalization of Cy3 and Cy5 attached to macromolecules measures intramolecular distances through time. *Proc. Natl. Acad. Sci. USA* 102, 1419–1423.
- Cougot, N., Cavalier, A., Thomas, D., and Gillet, R. (2012). The dual organization of P-bodies revealed by immunoelectron microscopy and electron tomography. *J. Mol. Biol.* 420, 17–28.
- Djuranovic, S., Nahvi, A., and Green, R. (2012). miRNA-mediated gene silencing by translational repression followed by mRNA deadenylation and decay. *Science* 336, 237–240.
- Eulalio, A., Behm-Ansmant, I., and Izaurralde, E. (2007a). P bodies: at the crossroads of post-transcriptional pathways. *Nat. Rev. Mol. Cell Biol.* 8, 9–22.
- Eulalio, A., Behm-Ansmant, I., Schweizer, D., and Izaurralde, E. (2007b). P-body formation is a consequence, not the cause, of RNA-mediated gene silencing. *Mol. Cell Biol.* 27, 3970–3981.
- Fusco, D., Accornero, N., Lavoie, B., Shenoy, S.M., Blanchard, J.M., Singer, R.H., and Bertrand, E. (2003). Single mRNA molecules demonstrate probabilistic movement in living mammalian cells. *Curr. Biol.* 13, 161–167.
- Grimm, J.B., English, B.P., Chen, J., Slaughter, J.P., Zhang, Z., Revyakin, A., Patel, R., Macklin, J.J., Normanno, D., Singer, R.H., et al. (2015). A general method to improve fluorophores for live-cell and single-molecule microscopy. *Nat. Methods* 12, 244–250, 3 p following 250.
- Grünwald, D., and Singer, R.H. (2010). In vivo imaging of labelled endogenous β -actin mRNA during nucleocytoplasmic transport. *Nature* 467, 604–607.
- Horvathova, I., Voigt, F., Kotrys, A.V., Zhan, Y., Artus-Revel, C.G., Eglinger, J., Stadler, M.B., Giorgetti, L., and Chao, J.A. (2017). The Dynamics of mRNA Turnover Revealed by Single-Molecule Imaging in Single Cells. *Mol. Cell* 68, 615–625.e9.
- Hosono, Y., Niknafs, Y.S., Prensner, J.R., Iyer, M.K., Dhanasekaran, S.M., Mehra, R., Pitchiaya, S., Tien, J., Escara-Wilke, J., Poliakov, A., et al. (2017). Oncogenic Role of THOR, a Conserved Cancer/Testis Long Non-coding RNA. *Cell* 171, 1559–1572.e20.
- Hubstenberger, A., Courel, M., Benard, M., Souquere, S., Ernoult-Lange, M., Chouaib, R., Yi, Z., Morlot, J.B., Munier, A., Fradet, M., et al. (2017). P-Body Purification Reveals the Condensation of Repressed mRNA Regulons. *Mol. Cell* 68, 144–157.e5.
- Huch, S., and Nissan, T. (2017). An mRNA decapping mutant deficient in P body assembly limits mRNA stabilization in response to osmotic stress. *Sci. Rep.* 7, 44395.
- Jakymiw, A., Lian, S., Eystathiou, T., Li, S., Satoh, M., Hamel, J.C., Fritzler, M.J., and Chan, E.K. (2005). Disruption of GW bodies impairs mammalian RNA interference. *Nat. Cell Biol.* 7, 1267–1274.
- Kedersha, N., and Anderson, P. (2007). Mammalian stress granules and processing bodies. *Methods Enzymol.* 431, 61–81.
- Kedersha, N., Tisdale, S., Hickman, T., and Anderson, P. (2008). Real-time and quantitative imaging of mammalian stress granules and processing bodies. *Methods Enzymol.* 448, 521–552.
- Khong, A., Matheny, T., Jain, S., Mitchell, S.F., Wheeler, J.R., and Parker, R. (2017). The Stress Granule Transcriptome Reveals Principles of mRNA Accumulation in Stress Granules. *Mol. Cell* 68, 808–820.e5.
- Leung, A.K., Calabrese, J.M., and Sharp, P.A. (2006). Quantitative analysis of Argonaute protein reveals microRNA-dependent localization to stress granules. *Proc. Natl. Acad. Sci. USA* 103, 18125–18130.
- Liu, J., Valencia-Sanchez, M.A., Hannon, G.J., and Parker, R. (2005). MicroRNA-dependent localization of targeted mRNAs to mammalian P-bodies. *Nat. Cell Biol.* 7, 719–723.
- Lytle, J.R., Yario, T.A., and Steitz, J.A. (2007). Target mRNAs are repressed as efficiently by microRNA-binding sites in the 5' UTR as in the 3' UTR. *Proc. Natl. Acad. Sci. USA* 104, 9667–9672.
- Martin, K.C., and Ephrussi, A. (2009). mRNA localization: gene expression in the spatial dimension. *Cell* 136, 719–730.
- Moon, S.L., Morisaki, T., Khong, A., Lyon, K., Parker, R., and Stasevich, T.J. (2019). Multicolour single-molecule tracking of mRNA interactions with RNP granules. *Nat. Cell Biol.* 21, 162–168.
- Mourão, M., Kreitman, D., and Schnell, S. (2014). Unravelling the impact of obstacles in diffusion and kinetics of an enzyme catalysed reaction. *Phys. Chem. Chem. Phys.* 16, 4492–4503.
- Parker, R., and Sheth, U. (2007). P bodies and the control of mRNA translation and degradation. *Mol. Cell* 25, 635–646.
- Pillai, R.S., Bhattacharyya, S.N., Artus, C.G., Zoller, T., Cougot, N., Basyuk, E., Bertrand, E., and Filipowicz, W. (2005). Inhibition of translational initiation by Let-7 MicroRNA in human cells. *Science* 309, 1573–1576.
- Pitchiaya, S., Androsavich, J.R., and Walter, N.G. (2012). Intracellular single molecule microscopy reveals two kinetically distinct pathways for microRNA assembly. *EMBO Rep.* 13, 709–715.
- Pitchiaya, S., Krishnan, V., Custer, T.C., and Walter, N.G. (2013). Dissecting non-coding RNA mechanisms in cellulo by Single-molecule High-Resolution Localization and Counting. *Methods* 63, 188–199.
- Pitchiaya, S., Heinicke, L.A., Custer, T.C., and Walter, N.G. (2014). Single molecule fluorescence approaches shed light on intracellular RNAs. *Chem. Rev.* 114, 3224–3265.
- Pitchiaya, S., Heinicke, L.A., Park, J.I., Cameron, E.L., and Walter, N.G. (2017). Resolving Subcellular miRNA Trafficking and Turnover at Single-Molecule Resolution. *Cell Rep.* 19, 630–642.

- Protter, D.S.W., and Parker, R. (2016). Principles and Properties of Stress Granules. *Trends Cell Biol.* 26, 668–679.
- Raj, A., van den Bogaard, P., Rifkin, S.A., van Oudenaarden, A., and Tyagi, S. (2008). Imaging individual mRNA molecules using multiple singly labeled probes. *Nat. Methods* 5, 877–879.
- Rueda, D., Bokinsky, G., Rhodes, M.M., Rust, M.J., Zhuang, X., and Walter, N.G. (2004). Single-molecule enzymology of RNA: essential functional groups impact catalysis from a distance. *Proc. Natl. Acad. Sci. USA* 101, 10066–10071.
- Schütz, S., Nöldeke, E.R., and Sprangers, R. (2017). A synergistic network of interactions promotes the formation of in vitro processing bodies and protects mRNA against decapping. *Nucleic Acids Res.* 45, 6911–6922.
- Shin, Y., and Brangwynne, C.P. (2017). Liquid phase condensation in cell physiology and disease. *Science* 357, eaaf4382.
- Shukla, S., Evans, J.R., Malik, R., Feng, F.Y., Dhanasekaran, S.M., Cao, X., Chen, G., Beer, D.G., Jiang, H., and Chinnaiyan, A.M. (2016). Development of a RNA-Seq Based Prognostic Signature in Lung Adenocarcinoma. *J. Natl. Cancer Inst.* 109, djw200.
- Simonson, P.D., Deberg, H.A., Ge, P., Alexander, J.K., Jeyifous, O., Green, W.N., and Selvin, P.R. (2010). Counting bungarotoxin binding sites of nicotinic acetylcholine receptors in mammalian cells with high signal/noise ratios. *Biophys. J.* 99, L81–L83.
- Spector, D.L. (2006). SnapShot: Cellular bodies. *Cell* 127, 1071.
- Stalder, L., and Mühlemann, O. (2009). Processing bodies are not required for mammalian nonsense-mediated mRNA decay. *RNA* 15, 1265–1273.
- Tutucci, E., Vera, M., Biswas, J., Garcia, J., Parker, R., and Singer, R.H. (2018). An improved MS2 system for accurate reporting of the mRNA life cycle. *Nat. Methods* 15, 81–89.
- Van Treeck, B., and Parker, R. (2018). Emerging Roles for Intermolecular RNA-RNA Interactions in RNP Assemblies. *Cell* 174, 791–802.
- Weidensdorfer, D., Stöhr, N., Baude, A., Lederer, M., Köhn, M., Schierhorn, A., Buchmeier, S., Wahle, E., and Hüttelmaier, S. (2009). Control of c-myc mRNA stability by IGF2BP1-associated cytoplasmic RNPs. *RNA* 15, 104–115.
- Wilbertz, J.H., Voigt, F., Horvathova, I., Roth, G., Zhan, Y., and Chao, J.A. (2019). Single-Molecule Imaging of mRNA Localization and Regulation during the Integrated Stress Response. *Mol. Cell*, S1097-2765(18)31036-0.
- Zhang, Y., Pitchiaya, S., Ciešlik, M., Niknafs, Y.S., Tien, J.C., Hosono, Y., Iyer, M.K., Yazdani, S., Subramaniam, S., Shukla, S.K., et al. (2018). Analysis of the androgen receptor-regulated lncRNA landscape identifies a role for ARLNC1 in prostate cancer progression. *Nat. Genet.* 50, 814–824.

STAR★METHODS

KEY RESOURCES TABLE

REAGENT or RESOURCE	SOURCE	IDENTIFIER
Antibodies		
Rabbit-anti-Dcp1a	Sigma	HPA013202
Rabbit-anti-Dcp2	Thermo	PIPA5-34455
Rabbit-anti-PUM	Abcam	EPR3795
Rabbit-anti-ELAVL1	Sigma	07-1735
Rabbit-anti-PABP	Abcam	ab21060
Rabbit-anti-eIF4E	Abcam	ab1126
Rabbit-anti-eIF4G	Sigma	07-1800
mouse-anti-rRNA	Novus Biologicals	NB100-662SS
Rabbit-anti-GAPDH	Cell signaling technol.	2118S
Rabbit-anti-Xrn1	Bethyl labs	A300-443A
Rabbit-anti-DDX6	Bethyl labs	A300-460A
Mouse-anti-GW182	Abcam	Ab70522
Rabbit-anti-Ago2	Sigma	07-590
Mouse-anti-G3BP	BD Transduction labs	611126
Rabbit-anti-CNOT1	Proteintech	14276-1-AP
Goat-anti-rabbit-Cy5	Jackson Immunolabs	111-175-144
Goat-anti-mouse-Cy5	Jackson Immunolabs	115-175-146
Chemicals, Peptides, and Recombinant Proteins		
JF646-HaloTag ligand	Lab of Luke Lavis,	N/A
Sodium Arsenite	Sigma	S7400-100G
Critical Commercial Assays		
MegaScript T7	Thermo-Fisher	AM1334
ScriptCap m7G Capping System	CELLSCRIPT	C-SCCE0625
A-Plus Poly(A) Polymerase Tailing Kit	CELLSCRIPT	C-PAP5104H
Fugene HD	Promega	E2311
Lipofectamine 2000	Thermo-Fisher	11668027
CellTiter-Glo® Luminescent Cell Viability Assay	Promega	G7570
Dual-Glo Luciferase Assay System	Promega	E2920
Deposited Data		
Unprocessed image files used to prepare the images	Mendeley Data	https://doi.org/10.17632/65t29ys57x.1
Experimental Models: Cell Lines		
Human: U2-OS	ATCC	HTB-96
Human: HeLa	ATCC	CCL-2
Human: HeLa stably expressing GFP-Dcp1a	This paper	N/A
Human: U2-OS stably expressing GFP-Dcp1a	This paper	N/A
Human: U2-OS stably expressing GFP-G3BP and RFP-Dcp1a	Nancy Kedersha	N/A
Oligonucleotides		
Labeled microRNAs for injection see Table S1	This paper	N/A
Primers and gene blocks for cloning see Table S1	This paper	N/A
Recombinant DNA		
pRL-TK-cx6x	Lab of Phil Sharp	Addgene: 11324
pRL-TK-let7-A	Lab of Phil Sharp	Addgene: 11325

(Continued on next page)

Continued

REAGENT or RESOURCE	SOURCE	IDENTIFIER
pRL-TK-let7-B	Lab of Phil Sharp	Addgene: 11308
pEF6-mCh-cx6x	Pitchiaya et al., 2017	N/A
pEF6-mCh-l7-6x	Pitchiaya et al., 2017	N/A
pEGFP-C1	Clontech	Discontinued
pmRFP1-hDcp1a	Nancy Kedersha	N/A
phage-ubc-nls-ha-2xmcp-HALO	Lab of Phil Sharp	Addgene: 64540
pmiR-GLO	Promega	E1330
pSL-MS2_24x	Lab of Robert Singer	Addgene: 31865
pmG-MS2	This paper	N/A
pmG-l7-6x	This paper	N/A
pmG-l7-6x-MS2	This paper	N/A
pmG-m17-6x	This paper	N/A
pmG-m17-6x-MS2	This paper	N/A
pmG-cx-6x	Pitchiaya et al., 2017	N/A
pmG-cx-6x-MS2	This paper	N/A
l7-6x-pmG	This paper	N/A
l7-6x-pmG-MS2	This paper	N/A
m17-6x-pmG	This paper	N/A
m17-6x-pmG-MS2	This paper	N/A
pmG-l7-2x-cx-4x	This paper	N/A
pmG-l7-2x-cx-4x-MS2	This paper	N/A
pLenti6-THOR	Hosono et al., 2017	N/A
pLenti6-RHOT	Hosono et al., 2017	N/A
pLenti6-THOR-MS2	This paper	N/A
pCDH-THOR-ΔIGF2BP1	This paper	N/A
pCDH-THOR-ΔIGF2BP1-MS2	This paper	N/A
pCDH-ARLNC1	Zhang et al., 2018	N/A
pCDH-ARLNC1-MS2	This paper	N/A
pCDH-LINC00941	This paper	N/A
pCDH-LINC00941-MS2	This paper	N/A
Software and Algorithms		
MATLAB 8.3	The Mathworks Inc.	R2014a
Prizm 7.04	GraphPad	Prizm 7.04
Origin 2018	OriginLab	Origin 2018
Imaris 9.1.0	Bitplane AG	Imaris 9.1.0
Fiji	ImageJ/NIH	Fiji
Custom MATLAB routines	This paper	N/A
Custom ImageJ macros	This paper	N/A
Bacterial and viral strains		
E.coli SURE2 Supercompetent Cells	Agilent	200152

CONTACT FOR REAGENT AND RESOURCE SHARING

Further information and requests for resources and reagents should be directed to and will be fulfilled by the Lead Contact, Nils G. Walter (nwalter@umich.edu) or co-corresponding author Sethuramasundaram Pitchiaya (sethu@umich.edu).

EXPERIMENTAL MODEL AND SUBJECT DETAILS

Cell lines

HeLa (CCI-2, ATCC) and U2-OS (HTB-96, ATCC) cells were propagated in DMEM (GIBCO, #11995) and McCoy's 5A (GIBCO, #16600) basal media respectively supplemented with 10% FBS (GIBCO, #16000). HeLa or U2-OS cells stably expressing GFP-Dcp1a (UGD) was created by transfecting U2-OS cells with pEGFP-Dcp1a and selecting for stable clones by G418 selection. UGD cells were grown in the abovementioned medium supplemented with 100 μ g/mL G418 (Thermo-Fisher, #10131027). All medium typically contained 1x Penicillin-Streptomycin (GIBCO, #15140). U2-OS cells stably expressing GFP-G3BP and RFP-Dcp1a (UGG-RD, gift from Nancy Kedersha) were propagated in McCoy's 5A (GIBCO, #16600) basal media supplemented with 10% FBS (GIBCO, #16000). Phenol-red free McCoy's 5A (GE-Amersham, #SH3027001) supplemented with 1% FBS was used for seeding and cells for imaging experiments. For hyperosmotic shock, cells were treated with the above media supplemented with 10 x PBS such that the final sodium concentration was 300 mM. Plasmid transfections for MS2-MCP imaging and cell growth assays were achieved using Fugene HD (Promega, #E2311). Cotransfection of plasmids with oligos was achieved using lipofectamine 2000 (Thermo-Fisher, #11668027). For inducing stress granules (SGs), growth media of UGG-RD cells were supplemented with 0.5mM Sodium Arsenite (NaAsO₂) for 1 h. All cell lines were subjected to biweekly mycoplasma contamination check and, HeLa and U2-OS cells were genotyped.

METHOD DETAILS

DNA, RNA and LNA oligonucleotides

All DNA and RNA oligonucleotides used for iShiRLoC experiments and reverse transcription, followed by quantitative polymerase chain reaction (RT-qPCR) were obtained from IDT. Oligonucleotides contained a 5' Phosphate (P) and, in the case of fluorophore labeled oligonucleotides, a Cy5 dye at the 3' end. Dyes were attached after oligonucleotide synthesis to a 3' amino group on a C6 carbon linker and were HPLC purified by the vendor. Guide and passenger strands were heat-annealed in a 1:1.1 ratio to achieve 10 μ M stock solutions and were frozen until further use. Negative control siRNA (Scr/Scr*) was purchased as ready-to-use duplex samples from Ambion respectively. Six tandem let-7 (l7-6x) miRNA response elements (MREs) or mutant l7-6x (ml7-6x) MREs were purchased as gene blocks from IDT. AntimiR LNA oligos were purchased from Exiqon. Oligonucleotide and gene block sequences are listed in [Table S1](#).

Plasmids

pEGFP-Dcp1a was constructed by ligating PCR amplified (using Pfu ultra polymerase, Agilent, #600380) EGFP ORF (from pEGFP-C1, Clontech) into pmRFP1-hDcp1a (gift from Nancy Kedersha, Brigham Women's hospital) within the AgeI and XhoI restriction enzyme (RE) sites. This replaces mRFP1 with EGFP in the plasmid. pEF6-mCh and pEF6-mCh-cx-6x construction was previously described previously ([Pitchiaya et al., 2017](#)). pEF6-mCh-l7-6x plasmid was constructed by ligating l7-6x gene block within NotI and XbaI sites of pEF6-mCh plasmid. Plasmids pRL-TK-let7-A, pRL-TK-let7-B, pRL-TK-cxcr4-6x, phage-ubc-nls-ha-2xmcp-HALO (a gift from Phil Sharp, Addgene plasmid #11324, #11325, #11308 and #64540) and pmIR-GLO (pmG, Promega, #E1330) were purchased. pmG-MS2, encoding the firefly luciferase (FL) gene followed by 24 MS2 stem loops (FL-MS2), was created in two steps. First, the coding sequence (CDS) of IF2 was PCR amplified and ligated into the SbfI and NotI RE site of pmG, to create pmG-IF2. MS2 stem loops from pSL-MS2_24x (a gift from Robert Singer, Addgene plasmid #31865) were then cloned into the EcoRI (introduced by above PCR)-NotI restriction enzyme sites pmG-IF2, to generate pmG-MS2. Clones containing the MS2 stem loops were created in SURE2 bacterial cells (Stratagene) to minimize recombination of the MS2 repeats with the bacterial genome. pmG-l7-6x-MS2 and pmG-ml7-6x-MS2 encoding FL-l7-6x-MS2 and FL-ml7-6x-MS2 respectively were constructed by ligating the l7-6x or ml7-6x gene blocks within the XhoI RE site in pmG-MS2. l7-6x-pmG and ml7-6x-pmG encoding l7-6x-FL and ml7-6x-FL respectively were created by ligating the synthesized l7-6x or ml7-6x fragment within the Esp3I and BbsI in pmG, between the human phosphoglycerate kinase promoter and FL CDS. l7-6x-pmG-MS2 and ml7-6x-pmG-MS2 encoding l7-6x-FL-MS2 and ml7-6x-FL-MS2 respectively were created using 24x MS2 stem loops from pmG-MS2 into EcoRI and NotI sites of l7-6x-pmG and ml7-6x-pmG. pmG-l7-2x-cx-4x was constructed by ligating the synthesized l7-2x-cx-4x fragment within the XhoI and EcoRI in pmG. pmG-l7-2x-cx-4x-MS2 was constructed by ligating 24x MS2 stem loops from pmG-MS2 into EcoRI and NotI sites of pmG-l7-2x-cx-4x. pmG-cx-6x-MS2 constructed by ligating 24x MS2 stem loops from pmG-MS2 into XhoI and NotI sites of pmG-cx-6x ([Pitchiaya et al., 2017](#)). pLenti6-THOR and pLenti6-RHOT (antisense of THOR) were constructed as described ([Hosono et al., 2017](#)). plenti6-THOR-MS2 was constructed by ligating 24x MS2 stem loops from pmG-MS2 into EcoRI and NotI sites of pLenti6-THOR. pCDH-ARinc1-MS2 was constructed by ligating 24x MS2 stem loops from pmG-MS2 into XhoI and NotI sites of pCDH-ARinc1 ([Zhang et al., 2018](#)). pCDH-LINC00941 was constructed by cloning LINC00941 into BstBI and BamHI sites of pCDH. pCDH-LINC00941-MS2 was then then constructed by ligating 24x MS2 stem loops from pmG-MS2 into XhoI and NotI sites of pCDH-LINC00941.

mRNA synthesis

pRL-TK-cx6x, pRL-TK-let7-A and pRL-TK-let7-B were linearized with NotI to generate RL-cx6x, RL-l7-2x and RL-ml7-2x mRNAs respectively. pEF6-mCh-cx6x and pEF6-mCh-l7-6x were linearized with XbaI to generate mCh-cx6x and mCh-l7-6x mRNA respectively. The pCFE-GFP plasmid (Thermo Scientific) was directly used in the *in vitro* transcription reactions to generate the GFP mRNA. The linearized plasmids were extracted with phenol and chloroform and subsequently ethanol precipitated. *In vitro* transcriptions were performed using the MegaScript T7 kit (Thermo-Fisher, # AM1334) according to manufacturer's protocol. Transcription reactions were then DNase treated (turbo DNase supplied with kit) and the respective RNAs were purified by sequential gel-filtration chromatography (Nap-5 followed by Nap-10, GE healthcare, # 17085301 and #17085401 respectively) and ethanol precipitation. The RNAs were 5' capped (ScriptCap m7G Capping System, CELLSERIP, # C-SCCE0625) and polyadenylated (A-Plus Poly(A) Polymerase Tailing Kit, CELLSERIP, # C-PAP5104H) and were further purified by sequential gel-filtration chromatography and ethanol precipitation. The length of the polyA tails was estimated based on electrophoretic mobility on a 1.2% formaldehyde agarose gel.

Luciferase reporter assays

100 μ L of 10,000–20,000 cells were seeded per well of a 96 well plate in antibiotics-free medium. Transfection conditions and luminescence readouts are as described previously (Pitchiaya et al., 2012; Pitchiaya et al., 2013; Pitchiaya et al., 2017). Briefly, cells were transfected with 60 ng of the indicated plasmid, 10 nM of the indicated dsRNA, and when appropriate 30 nM anti-ctrl or anti-l7 anti-miRs, 0.4 μ L of Lipofectamine 2000 (Invitrogen) and 50 μ L of OptiMEM (GIBCO). 6 h after transfection the growth medium was replaced with fresh medium. 24 h after transfection, medium was replaced with phenol red-free McCoy's 5A. Dual luciferase assays were performed using the Dual-Glo luciferase assay reagents (Promega, # E2920) as per the manufacturer's protocol and luminescence was detected using a Genios Pro (Tecan) plate reader.

RT-qPCR

Cells were harvested and total RNA from cells were isolated using QIAzol Lysis reagent (QIAGEN) and the miRNeasy kit (QIAGEN) with DNase digestion according to the manufacturer's instructions. cDNA was synthesized using Superscript III (Invitrogen) and random primers (Invitrogen). Relative RNA levels determined by qRT-PCR were measured on an Applied Biosystems 7900HT Real-Time PCR System, using Power SYBR Green MasterMix (Applied Biosystems). Expression was quantified by $2^{-\Delta C_t}$ method, wherein Myc expression was first normalized to that of GAPDH and then this normalized expression was further normalized to Mock treatment.

Cell growth assays

100 μ L of 10,000–20,000 cells were seeded per well of a 96 well plate in antibiotics-free medium and were transfected every 24 h with the appropriate plasmid construct using Eugene HD (Promega, # E2311). Cell growth and viability was measured as an end point measurement for each time point using the Cell-titer GLO assay (Promega, # G7570) based on manufacturer's instructions.

Microinjection

Cells grown on DeltaT dishes (Biotechs, # 0420042105C) were microinjected as described (Pitchiaya et al., 2012, 2013, 2017). Briefly, injection solutions contained the appropriate miRNA at 1 μ M concentration, 1x PBS and 0.5 mg/mL of 10 kDa cascade blue conjugated dextran (CB-Dex, Thermo-Fisher, # D1976). For microinjection based titration assays solution with 0–0.1 μ M, 1x PBS and 0.1 mg/mL of 500 kDa cascade blue conjugated dextran (FITC-Dex, Thermo-Fisher, # D7136). For microinjection based miRNA activity assay, mRNAs were added at a stoichiometric amount based on the number of miRNA binding sites, for instance, 0.16 μ M of RL-cx6x mRNA, bearing 6 cxcr4 binding sites, was added along with 1 μ M cxcr4 miRNA. Solutions were filtered through a 0.45 μ m Ultrafree-MC filter (Millipore, # UFC30HV00) and then centrifuged at 16,000 \times g for 15 min at 4°C immediately before injection. The solution was loaded into a femtotip (Eppendorf, # E5242952008). Injections were performed using a Femtojet pump (Eppendorf) and an Injectman (Eppendorf) mounted to the microscope. Microinjections were performed at 100 hPa injection pressure for 0.5 s with 20 hPa compensation pressure. This pressure translates to a volume of 0.02 pL and 10,000–20,000 miRNA molecules.

Single-molecule fluorescence *in situ* hybridization

smFISH was performed as described (Hosono et al., 2017). Briefly, cells were grown on 8-well chambered coverglasses (Thermo-Fisher, # 155383PK), formaldehyde fixed and permeabilized overnight at 4°C using 70% ethanol. Cells were rehydrated in a solution containing 10% formamide and 2 \times SSC for 5 min and then treated with 100 nM fluorescence *in situ* hybridization probes (LGC-Bioscience) for 16 h in 2 \times SSC containing 10% dextran sulfate, 2 mM vanadyl-ribonucleoside complex, 0.02% RNase-free BSA, 1 μ g μ L⁻¹ *E. coli* transfer RNA and 10% formamide at 37°C. After hybridization, cells were washed twice for 30 min at 37°C using a wash buffer (10% formamide in 2 \times SSC). Cells were then mounted in solution containing 10 mM Tris/HCl pH 7.5, 2 \times SSC, 2 mM trolox, 50 μ M protocatechuic acid and 50 nM protocatechuic dehydrogenase. Mounts were overlaid with mineral oil and samples were imaged immediately. Sequences of Q670 labeled probes against the FL gene are listed in Table S1 and probes against THOR and ARlnc1 were previously described (Hosono et al., 2017 and Zhang et al., 2018).

Immunofluorescence

Cells were grown on 8-well chambered coverglasses (Thermo-Fisher, # 155383PK), formaldehyde fixed and permeabilized using 0.5% Triton X-100 (Sigma, T8787-100ML) in 1x PBS at room temperature (RT) for 10 min. Cells were then treated with blocking buffer containing 5% normal goat serum (Jackson ImmunoResearch, 005-000-121), 0.1% Tween-20 (Sigma, P9416-50ML) in 1x PBS at RT for 1 h. Primary antibodies (pA) were diluted in blocking buffer to appropriate concentrations and cells were treated with pA at RT for 1 h. Following three washes with the blocking buffer for 5 min each cells were treated with secondary antibodies (sA) diluted in blocking buffer to appropriate concentrations. Following two washes with the blocking buffer and two washes with 1x PBS for 5 min each, cells were mounted in solution containing 10 mM Tris/HCl pH 7.5, 2 × SSC, 2 mM trolox, 50 μM protocatechuic acid and 50 nM protocatechuic dehydrogenase. Mounts were overlaid with mineral oil and samples were imaged immediately.

Microscopy

Highly inclined laminated optical sheet (HILO) imaging was performed as described (Pitchiaya et al., 2012; Pitchiaya et al., 2013; Pitchiaya et al., 2017) using a cell-TIRF system based on an Olympus IX81 microscope equipped with a 60x 1.49 NA oil-immersion objective (Olympus), as well as 405 nm (Coherent ©, 100 mW at source, ~65 μW for imaging CB-Dex), 488 nm (Coherent ©, 100 mW at source, ~1.2 mW for imaging GFP), 561 nm (Coherent ©, 100 mW at source, ~50 μW for imaging mCh) and 640 nm (Coherent ©, 100 mW at source, 13.5 mW for imaging Cy5) solid-state lasers. Quad-band filter cubes consisting of z405/488/532/640rpc or z405/488/561/640rpc dichroic filters (Chroma) and z405/488/532/640 m or z405/488/561/640 m emission filters (Chroma) were used to filter fluorescence of the appropriate fluorophores from incident light. Emission from individual fluorophores was detected sequentially on an EMCCD camera (Andor IXon Ultra) for fixed cell imaging. For multicolor live-cell imaging, the emitted light was split onto two different EMCCDs using a single beamsplitter within a filter adaptor (TuCam, Andor). Emission filters were placed just prior to each camera to minimize fluorescence bleed-through. For simultaneous detection of GFP and Cy5, a filter set with a 585dxcru dichroic that splits fluorescence into et525/50 m and et705/100 m emission filters respectively was placed in the Tucam adaptor. For live cell imaging of MS2-MCP constructs, UGD cells on Delta T dishes were treated with 100 nM JF646- Halo ligand (a kind gift from Luke Lavis) for 30 min in growth medium without phenol red (Grimm et al., 2015). After the treatment, cells were washed three times in media and placed back in the incubator for 30 min, prior to imaging.

Image analysis

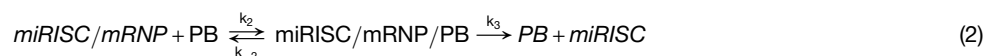
The two cameras used for simultaneous acquisition of GFP and Cy5 fluorescence in live cells were first registered as described (Churchman et al., 2005). Registration was achieved by imaging 0.1 μm tetraspeck beads (Thermo-Fisher, # T7279), whose emission is similar to both GFP and Cy5, before or after imaging of live cells. The registration matrix was then applied to GFP and Cy5 images for accurate tracking of PBs and RNAs respectively. Single particle tracking was performed as described (Pitchiaya et al., 2012; Pitchiaya et al., 2013) with some minor modifications. Briefly, particle tracking analysis was performed in Imaris (Bitplane) using tracks that spanned at least four video frames and all tracks were fit to a Brownian diffusion model to extract diffusion coefficients. PB boundaries were detected using a local contrast/threshold approach in ImageJ and Imaris. An RNA particle was identified as colocalizing with a PB when the centroid of the RNA is at or within the boundary of a PB. The use of finite observation windows to measure the dwell times introduces a systematic bias in the observed dwell times. This was corrected for by measuring the aggregate time for Cy5 photobleaching (T_{phb}) and subtracting its reciprocal this from the reciprocal of the observed dwell time (T_{obs}) along with the reciprocal of the observation window (T_w), as described by $T_{actual} = 1 / ((1/T_{obs}) - (1/T_{phb}) - (1/T_w))$, as described (Rueda et al., 2004). Dwell times of all transcripts are summarized in Table S2. Percentage of track colocalizing with PBs (track %) was calculated as $n_{PB} / (n_{PB} + n_{Cyt})$, where n_{PB} = number of track localizations within PBs, n_{Cyt} = number of track localizations in the cytosol and depicted in Figure 2. This measure, in addition to visual inspection of individual tracks were used to objectively define trajectory “phenotypes” as stable or transient.

Stepwise photobleaching analysis of fluorophore labeled miRNAs and intensity analysis of smFISH particles in fixed cells were done using custom written Lab-view codes and ImageJ macros that can be shared upon request, as described (Pitchiaya et al., 2012; Hosono et al., 2017). To overcome statistical biases of co-incidental colocalizations introduced merely by RNA abundance, we calculated the accumulation of RNA within PBs via an enrichment index (EI) – a ratio of the number of RNA molecules in PB to those outside of PBs (Figures 2 and S2). An E.I. of > 1 suggests that the RNA accumulates at PB, whereas the opposite is true if the E.I. is ≤ 1. We also calculated the percentage of RNA or protein signal within PBs per cell by calculating the ratio between the cumulative abundance of signal within PBs divided by the total signal within the cell. Mean abundance / cell of all transcripts are provided in Table S3. Relative localization (RL) of RNAs within PBs was calculated as $d_{CR} / (d_{RB} + d_{CB})$, where d_{CR} = distance of RNA centroid from PB centroid, d_{RB} = distance of RNA centroid from PB boundary, d_{CB} = distance of PB centroid from PB boundary and depicted in Figure S2. The centroid and boundary of PBs were obtained via a modest variation of the local/adaptive-threshold method previously described (Simonson et al., 2010).

mCh and GFP signal from microinjection based miRNA activity assay were extracted and analyzed as described (Pitchiaya et al., 2012; Pitchiaya et al., 2017). Briefly, mCh and GFP intensity threshold were set (Huang threshold in ImageJ) to automatically identify cell boundary. Background intensity, outside of cell boundary, was subtracted from mCh and GFP signal to extract the corrected intensity, whose ratio was calculated on a per cell basis.

In silico kinetic modeling

The fundamental theory and basic methodology of modeling, including the lattice gas automata algorithm are as described (Mourão et al., 2014). Our simulation platform allows for the specification of a variable number of elementary reactions. Unless otherwise stated, the results presented here were obtained using two different reactions:



The reaction in (2) represents a catalytic event. The rate coefficients k_i are modeled as reaction probabilities. For example, in (1) k_1 is modeled by the probability that a miRISC and an mRNP molecule will react to form complex miRISC/mRNP, given that they have collided. Unless otherwise stated, the probability of a forward reaction (on the basis of the rate coefficients k_1 and k_2) is set to 1 and the probability of a reverse reaction (on the basis of the rate coefficients k_{-1} and k_{-2}) is set to 0.1. The probability of a catalytic reaction (on the basis of the rate coefficient k_3) is set to 0.1. Note that the forward reaction rates (e.g., k_1) may remain constant over time, in agreement with the law of mass action, or decay over time for diffusion-limited reactions, when the time required for any two reactants to interact increases with the level of obstruction to diffusion. In the latter case, it can be shown that $\log(k_1)$ decays linearly at long times in a logarithmic timescale, as described (Mourão et al., 2014).

Each simulation begins with all particles randomly placed on a 2D lattice of size 200x200 lattice points with cyclic boundary conditions. Particles can be initialized with different sizes, provided that they are square, i.e., each initial particle can only occupy x^2 positions, x being at least 1. Our platform allows for the creation of initial aggregates of a particular number and size. With the restriction mentioned above, we modulate the number and size of P-body particles within an aggregate with the assumption that all P-body particles within an aggregate have the same size. Each aggregate of P-bodies is created in two main steps. In the first step occurs, we insert the first molecule of the aggregate in the lattice. This first molecule is placed in a random position in the lattice. In the second step, we randomly select an adjacent neighborhood of a random P-body in the existing aggregate as a destination for the new P-body. The addition of P-bodies to an aggregate follows the reaction:



where N_1 corresponds to the number of P-bodies in the existing aggregate. This is done iteratively until the pre-determined aggregated size is achieved. Every particle is randomly initialized with a given orientation and direction of rotation. There are six possible orientations, corresponding to the coordinate number of a triangular lattice. The direction of rotation is always clockwise (CW) or counter-clockwise (CCW). Note that, although the particle's movement is independent of its orientation, reactant particles will only associate if their orientations are complementary.

QUANTIFICATION AND STATISTICAL ANALYSIS

Graphpad-Prizm and Origin were used for statistical analysis and plotting. For pairwise comparisons, p values were calculated based on non-parametric unpaired t tests with Kolmogorov-Smirnov test. For comparisons involving more than 2 samples, one-way-ANOVA tests were used with Geisser-Greenhouse correction.

DATA AND SOFTWARE AVAILABILITY

Raw image files pertaining to figure panels in the main text and supplementary information can be found at Mendeley Data: <https://doi.org/10.17632/65t29ys57x.1>.

Molecular Cell, Volume 74

Supplemental Information

Dynamic Recruitment of Single RNAs to Processing Bodies Depends on RNA Functionality

Sethuramasundaram Pitchiaya, Marcio D.A. Mourao, Ameya P. Jalihal, Lanbo Xiao, Xia Jiang, Arul M. Chinnaiyan, Santiago Schnell, and Nils G. Walter

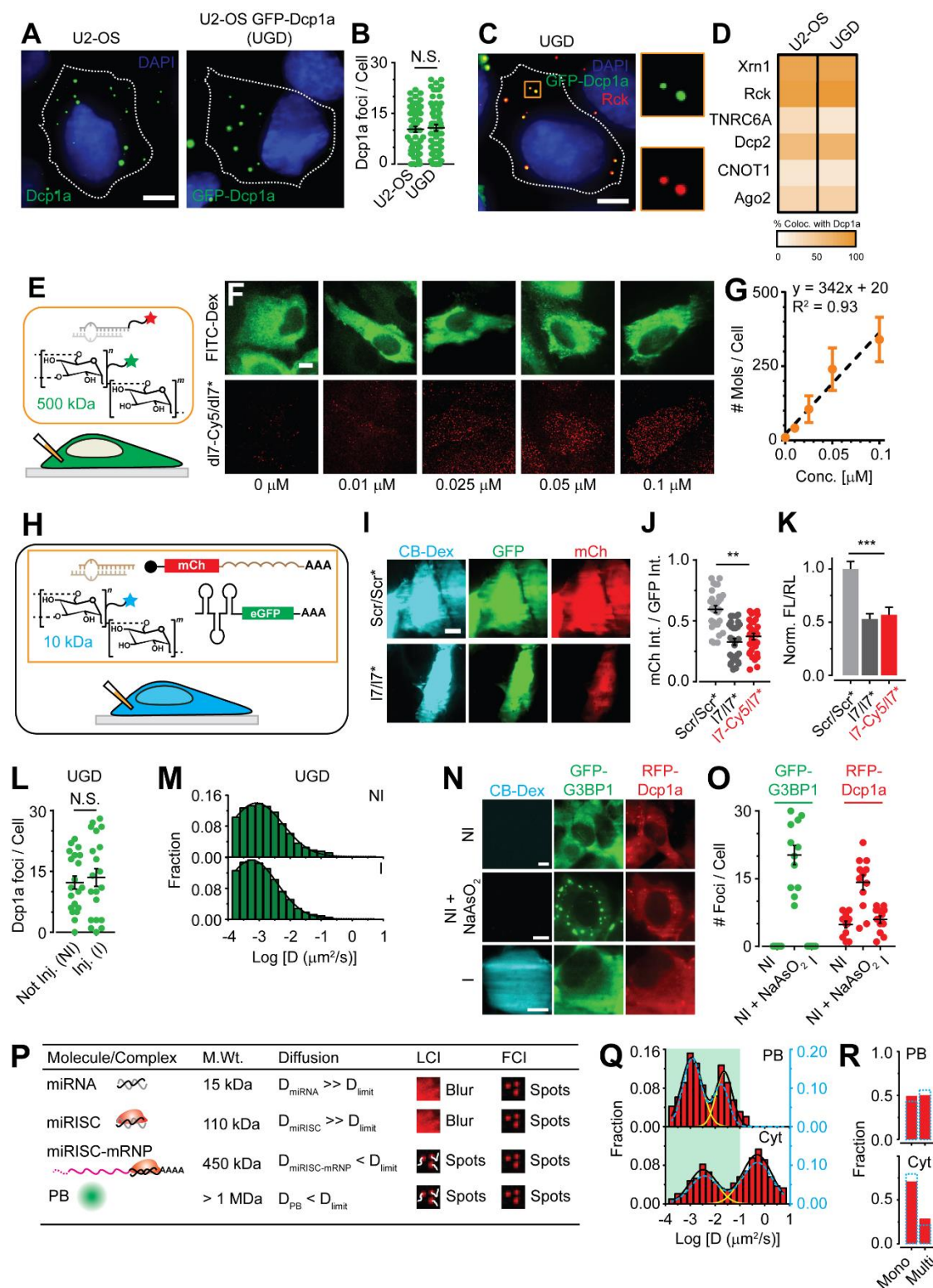


Figure S1. Validation of *in situ* miRNA imaging system (Related to Figure 1). (A)

Representative pseudocolored and contrast-adjusted images of U2-OS cells stained for

endogenous Dcp1a (green) via immunofluorescence and UGD cells expressing GFP-Dcp1a (green). Nucleus is stained with DAPI (blue). Dotted line, cell outline. Scale bar, 10 μ m. (B) Scatter plot depicting the number of endogenous Dcp1a or GFP-Dcp1a foci in U2-OS and UGD cells respectively ($n = 3$, 60 cells, N.S., not significant based on two-tailed, unpaired Student's t-test). (C) Representative pseudocolored and contrast-adjusted image of UGD cells expressing GFP-Dcp1a (green) and stained for Rck (red). Nucleus is stained with DAPI (blue). Dotted line, cell outline. Scale bar, 10 μ m. Orange $5.3 \times 5.3 \mu\text{m}^2$ inset is zoomed out and deconvolved into individual colors. (D) Mean colocalization percentage of endogenous Dcp1a foci from U2-OS cells or GFP-Dcp1a from UGD cells respectively, with other PB markers. Color coded scale-bar is also depicted ($n = 3$, ≥ 15 cells per sample). (E-G) Microinjection-based titration assay. (E) Schematic of microinjection setup, wherein Cy5 labeled double stranded DNA (dl7-Cy5/dl7*, red) bearing the same sequence as l7-Cy5/l7* miRNA was co-microinjected along with 500 kDa FITC-Dextran (green), exclusively localizes to the cytosol. (F) Representative pseudocolored and contrast-adjusted images of U2-OS cells microinjected with various concentrations of dl7-Cy5/dl7*. Scale bar, 10 μ m. (G) Plot depicting the relationship between dl7-Cy5/dl7* concentration (Conc., μ M) in the microinjection solution and the number of molecules detected per cell (# Mols / Cell). Dotted line represents fitted line. Equation of fitted line and goodness of fit (R^2) are also depicted. (H-K) miRNA activity assays. (H) Schematic of microinjection-based miRNA activity assay. (I) Representative pseudocolored and contrast-adjusted image of U2-OS cells expressing mCherry (mCh, red) reporter gene and GFP normalization gene (green), also containing 10 kDa cascade-blue dextran (CB-Dex, cyan) and the miRNA (Scr/Scr* -

scrambled control, I7/I7* - let-7 miRNA) of interest. Scale bar, 10 μ m. (J) Scatter plot depicting the mCh : GFP intensity ratio for various conditions (n = 3 replicates, total 30 cells; **p < 0.001 based on two-tailed, unpaired Student's t-test). Mean and s.e.m are depicted. (K) Luciferase reporter assays represented as the ratio of luminescence from a firefly luciferase (FL) reporter gene containing 6x let-7 MREs (FL-I7-6x) and a renilla luciferase (RL) normalization gene in U2-OS cells (n = 12 replicates, ***p < 0.0001 based on two-tailed, unpaired Student's t-test). Mean and s.e.m are depicted. (L-O) Microinjection does not affect sub-cellular behavior of PBs and does not induce stress granules. Number (L) and diffusion constants (M) of PBs in cells that were not injected (Not Inj., NI) or injected (Inj., I). Representative pseudocolored and contrast-adjusted images of U2-OS cells stably expressing GFP-G3BP (green), a stress granule (SG) marker, and RFP-Dcp1a (red), which were not injected (NI), treated with sodium arsenite (NI + NaAsO₂) or co-injected with CB-Dex (cyan) and I7-Cy5/I7* are shown in N. Scale bar, 10 μ m. Quantification of the number of GFP or RFP foci per cell is shown in O. (P) Expected phenotype of distinct molecular species in iSHIRLoC assays. LCI, live cell imaging; FCI, fixed cell imaging. (Q-R) Dynamics and stoichiometry of I7-Cy5/I7* in GFP-Dcp1a expressing HeLa cells are almost identical to those in UGD cells. (Q) Distribution of I7-Cy5/I7* miRNA diffusion constants in PB and Cyt within living HeLa cells that are expressing GFP-Dcp1a. Green area on the plot depicts the range of PB diffusion constants (n = 3, 13 cells). Dotted blue line represents distribution of I7-Cy5/I7* miRNA diffusion constants within UGD cells, as in Figure 1D. (R) Distribution of I7-Cy5/I7* miRNA stoichiometry as monomeric (Mono, 1 photobleaching step) or multimeric (Multi, \geq 2 photobleaching steps) complexes in PB and Cyt within fixed HeLa cells that are

expressing GFP-Dcp1a ($n = 4$, 21 cells). Dotted blue line represents stoichiometry in UGD cells, as in Figure 1F.

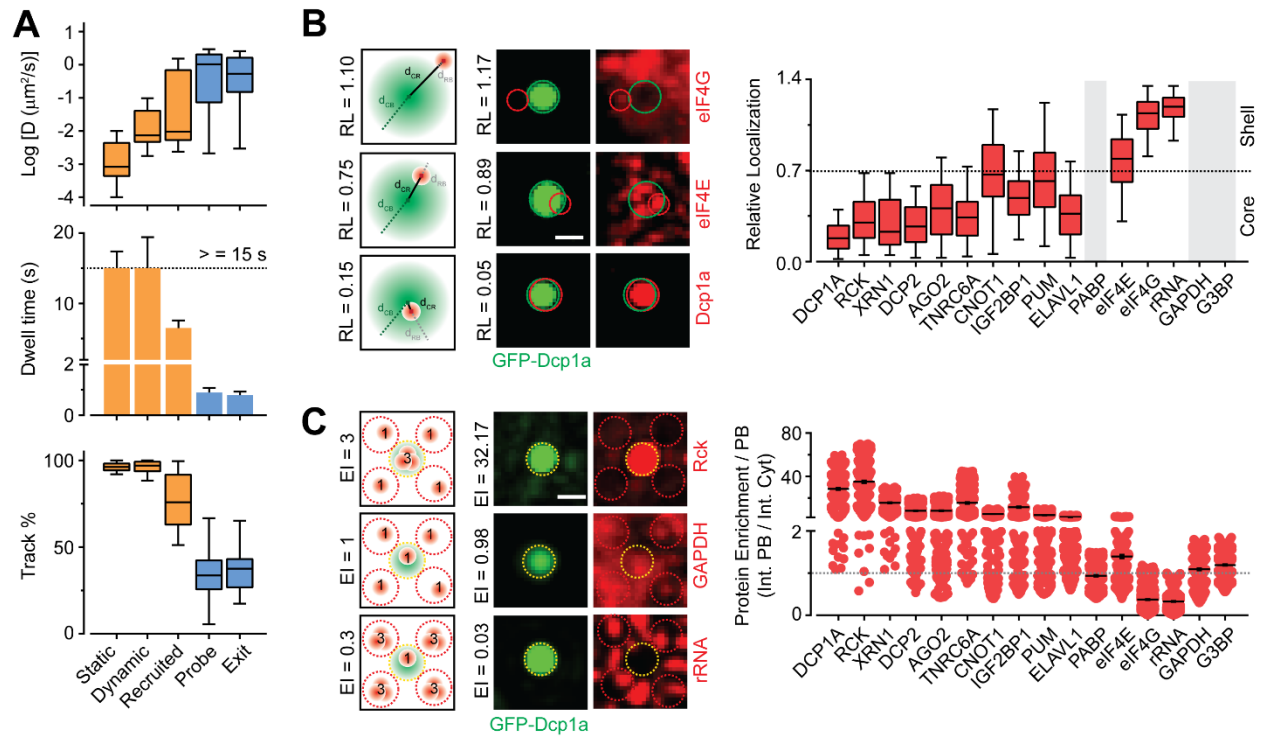


Figure S2. Characterization of miRNA-PB interaction modes and localization patterns (Related to Figure 2). (A) Distribution of diffusion constants (top), Dwell time statistics (middle) and distribution of the percentage of track length colocalizing with PB (bottom) for each RNA-PB interaction type. Dotted black line represents duration of acquisition. Photobleaching corrected dwell times that were greater than acquisition window were rounded to the acquisition time span ($n = 3, 15$ cells). (B) Schematic (left) of relative localization (RL) calculation. d_{CR} = distance of RNA centroid from PB centroid, d_{RB} = distance of RNA centroid from PB boundary, d_{CB} = distance of PB centroid from PB boundary. Representative pseudocolored and contrast-adjusted regions of UGD cells (middle) with GFP-Dcp1a (green), stained for eIF4G, eIF4E or Dcp1a (red). Green and red dotted circles represent boundaries of PBs and Rck particles respectively. Scale bar, 2 μm . Relative localization values of top and bottom panels are represented within the images. Distribution of protein localization relative to GFP-Dcp1a, which were used to

define PB center and boundary ($n = 3, \geq 15$ cells per sample). Black dotted line represents the RL limit for core localizations. Grey boxes denotes the protein factors which were evenly dispersed across the entire cytosol and consequently did not have any detectable features (local maxima) for RL calculations. (C) Schematic (left) of enrichment index (EI) calculation. Representative pseudocolored and contrast-adjusted regions of UGD cells (middle) with GFP-Dcp1a (green), stained for Rck, GAPDH or rRNA (red,). Yellow and red dotted circles represent PB-localized and cytoplasmic signal respectively. Scale bar, 2 μm . EI of top and bottom panels are represented within the images. Scatter plot of EI (right) for IF signal at PBs. Each dot represents an individual PB colocalization event ($n = 3, \geq 15$ cells per sample). Grey dotted line depicts an EI of one, which demarcates PB-enriched (> 1) from PB-depleted (< 1) factors.

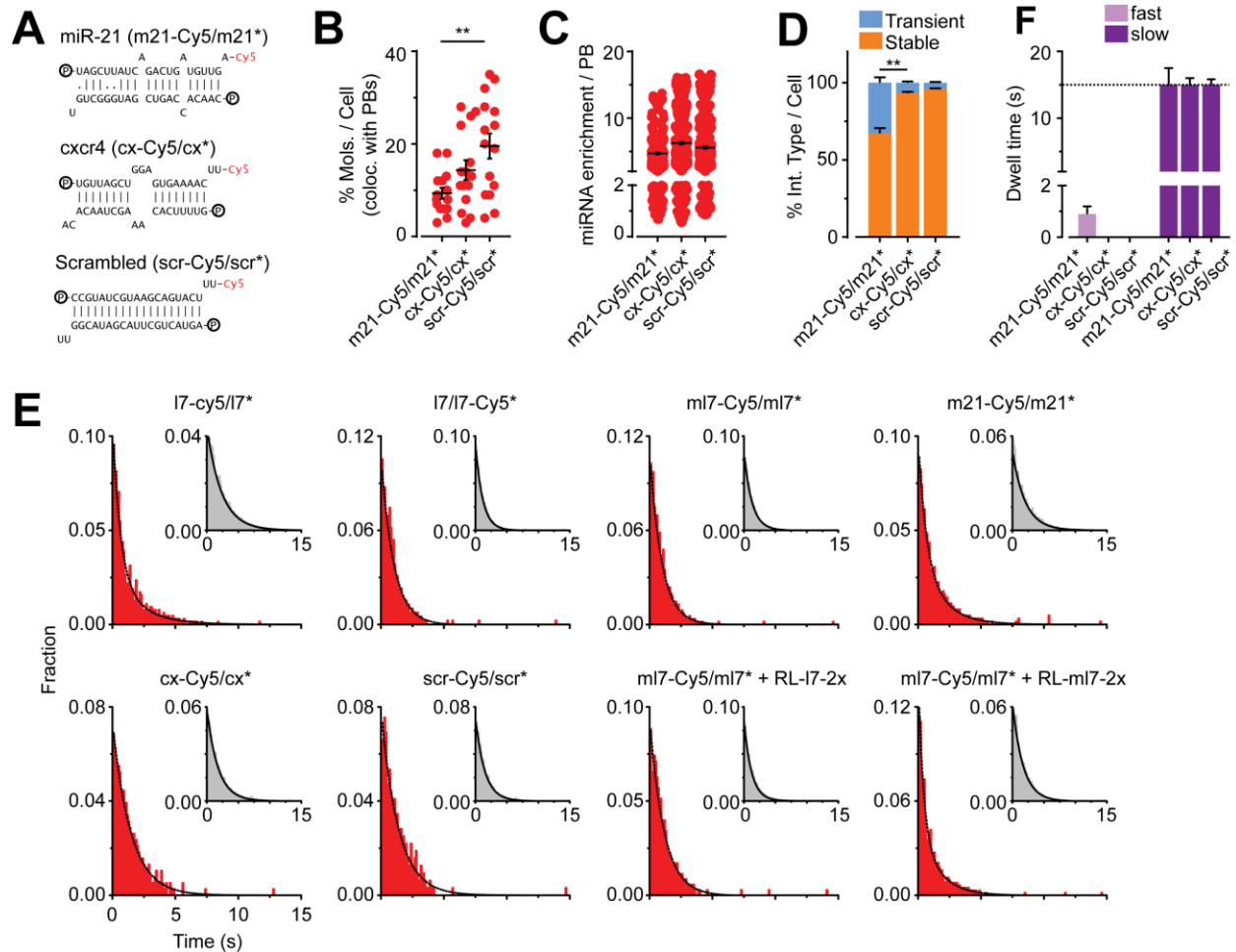


Figure S3. PB-localization and interaction kinetics of different miRNAs, in the presence or absence of cognate targets (Related to Figure 3). (A) Schematic of additional miRNAs used. P, lines and dots represent 5' phosphate, Watson-crick base pairing and wobble pairing respectively. (B) Scatter plot representing the % of miRNA molecules that colocalize with PBs per fixed UGD cell. Each dot represents a cell. (C) Scatter plot of EI for different constructs. Each dot represents an individual miRNA-PB colocalization event in fixed UGD cells. (D) Relative distribution of stable and transient interactions per live UGD cell for different miRNAs. (E) Dwell time distribution of all miRNAs at PBs in live UGD cells. Black line depicts single or double exponential fit. Inset,

dwell time distribution of miRNAs inside cells, prior to photobleaching. Black line depicts single exponential fit. (F) Comparison of fast and slow miRNA-PB interaction kinetics for the additional miRNAs in live UGD cells. ($n \geq 3$; ≥ 15 cells, $**p \leq 0.001$ by two-tailed, unpaired Student's t-test.).

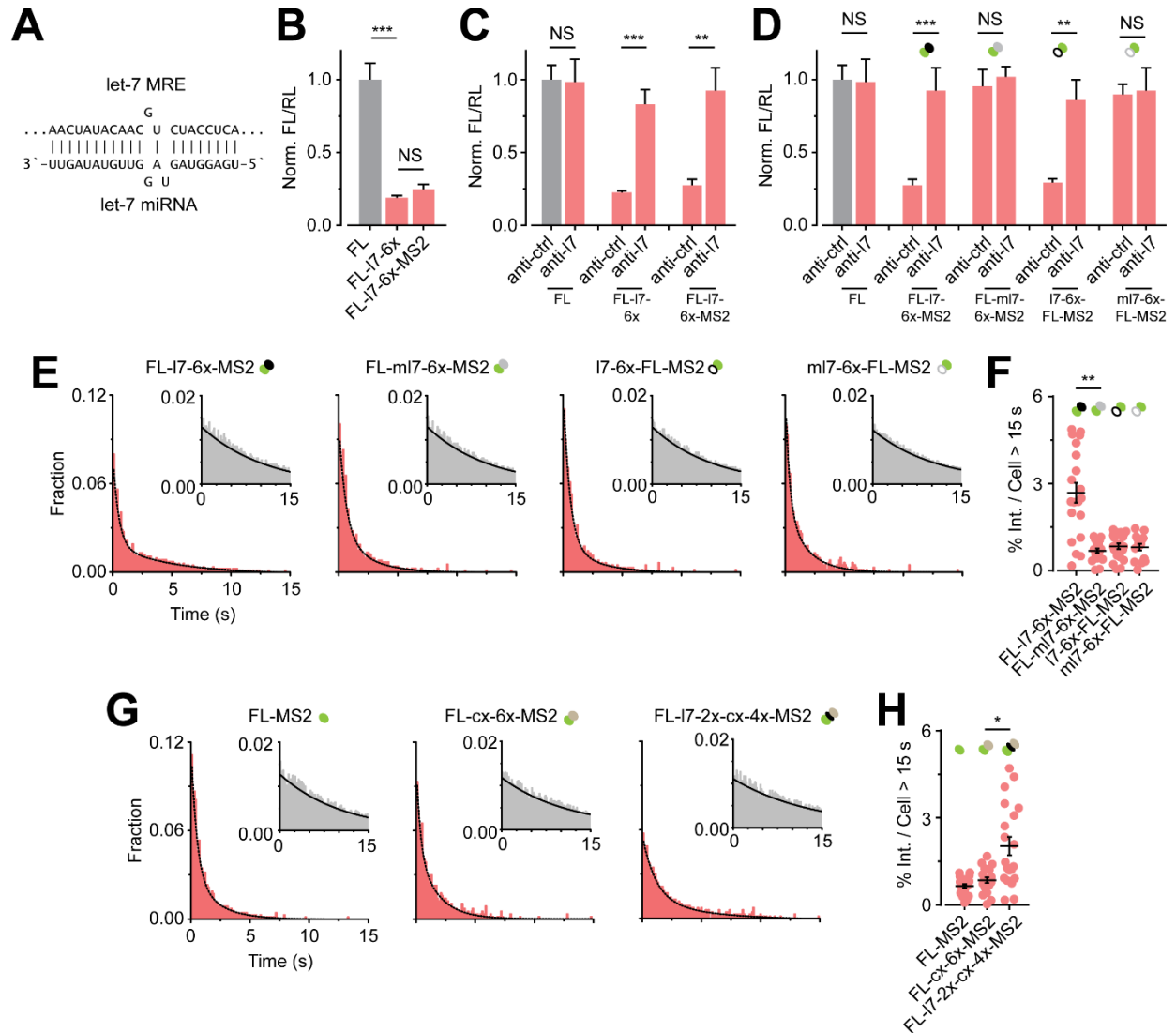


Figure S4. Validation of *in situ* m/lncRNA imaging system (Related to Figure 4). (A)

Luciferase reporter assays of the appropriate mRNA constructs (n = 12). Data were normalized to FL. Mean and s.e.m are depicted (n = 12 replicates, NS = not significant or ***p < 0.0001 based on two-tailed, unpaired Student's t-test). (B-C) Luciferase reporter assays of the appropriate mRNA constructs treated with a control anti-miR (anti-ctrl) or an anti-let7 (anti-I7) anti-miR. (n = 12). Data were normalized to FL (anti-ctrl). Mean and s.e.m are depicted (n = 12 replicates, NS = not significant, **p ≤ 0.001 or ***p < 0.0001 based on two-tailed, unpaired Student's t-test). (D and F) Dwell time distribution of the

appropriate mRNA constructs at PBs. Black line depicts double exponential fit Inset, dwell time distribution of mRNAs inside cells, prior to photobleaching. Black line depicts single exponential fit. (E and G) Scatter plot representing % of mRNA-PB interactions that last for the entire duration of imaging (15 s), without photobleaching, per live UGD cell. $n = 3$, ≥ 15 cells per sample, $**p < 0.001$ based on two-tailed, unpaired Student's t-test.

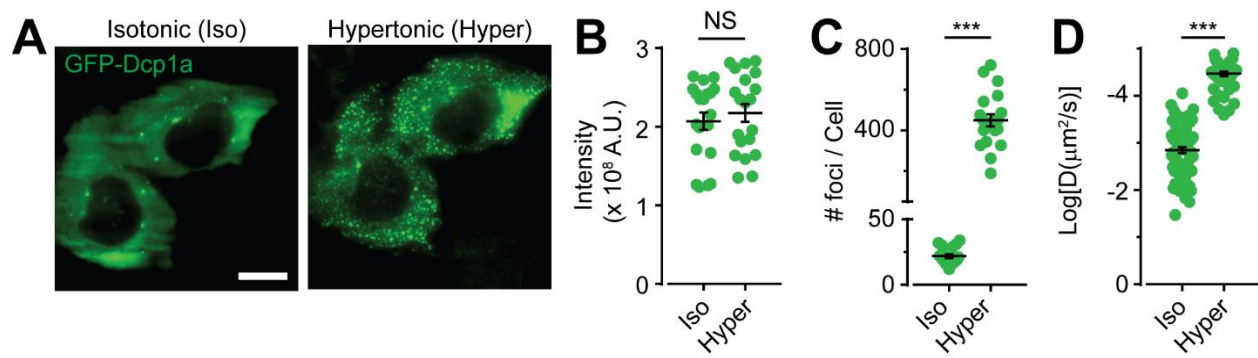


Figure S5. Characterization of cells treated with hyper-osmotic medium (Related to Figure 5). (A) Representative pseudocolored images of UGD cells treated with isotonic or hypertonic media. GFP-Dcp1a, green. Scale bar, 10 μm . (B-D) Scatter plot of the intensity per cell (B), number of GFP foci per cell (C) and diffusion coefficients of PBs (D) under each treatment condition. $n = 3$, 20 cells per sample, NS = not significant or *** $p < 0.001$ based on two-tailed, unpaired Student's t-test.

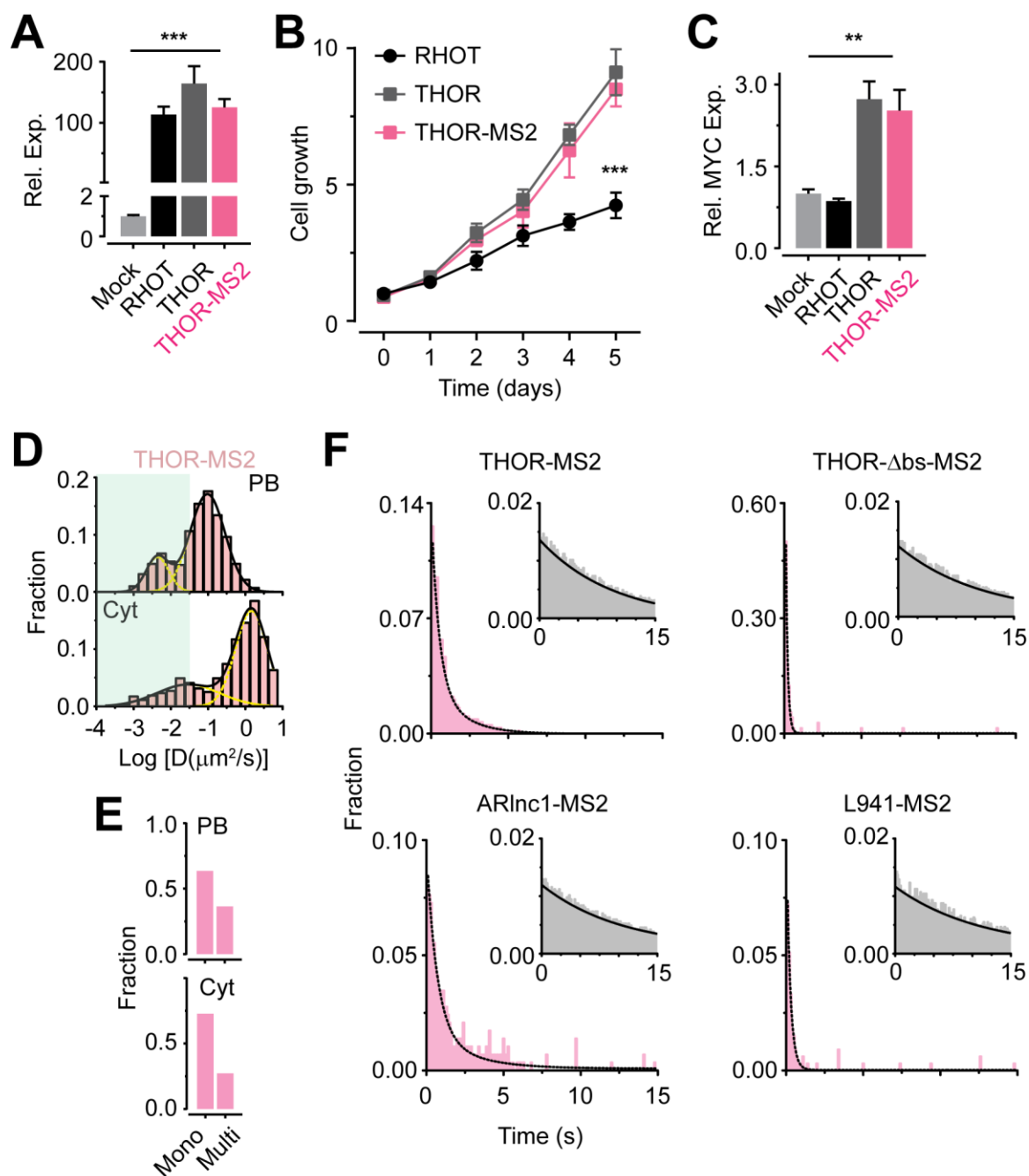


Figure S6. IncRNA construct validation and kinetics (Related to Figure 6). (A)

Relative expression of the appropriate IncRNA constructs transfected into UGD cells as measured by RT-qPCR and normalized to mock. (B) Cell growth as measured by ATP abundance in UGD cells transfected with the appropriate IncRNA construct (C) Relative expression of MYC in UGD cells transfected with IncRNA constructs, as measured by RT-

qPCR and normalized to mock. Mean and s.e.m are depicted for A-C. $n = 3$ replicates, $**p < 0.0001$ based on two-tailed, unpaired Student's t-test. (D) Distribution of THOR-MS2 lncRNA diffusion constants in PB and Cyt within live UGD cells. (E) Distribution of THOR-MS2 lncRNA stoichiometry as monomeric or multimeric complexes in PB and Cyt within fixed UGD cells. (F) Dwell time distribution of all lncRNAs at PBs in live UGD cells. Black line depicts single or double exponential fit. Inset, dwell time distribution of lncRNAs inside cells, prior to photobleaching. Black line depicts single exponential fit. $n = 3$, 20 cells.

Table S1. Sequences of oligonucleotides.

Related to Figures 1-6 and Figures S1-S4 and S6.

Name	DNA/ RNA	Sequence
l7	RNA	P-UGAGGUAGUAGGUUGUAUAGUU-X
l7*	RNA	P-CUAUACAAUCUACUGUCUUUCC-X
dl7	DNA	P-TGAGGTAGTAGGTTGTATAGTT-X
dl7*	DNA	P-CTATACAATCTACTGTCTTTCC-X
ml7	RNA	P-UGCGUUAGUAGGUUGUAUAGUU-X
ml7*	RNA	P-CUAUACAAUCUACUGUCGUUCC-X
m21	RNA	P-UAGCUUAUCAGACUGAUGUUGA-X
m21*	RNA	P-CAACACCAGUCGAUGGGCUGU-X
cx	RNA	P-UGUUAGCUGGAGUGAAAACUU-X
cx*	RNA	P-GUUUUCACAAAGCUAACACA-X
Scr	RNA	P-CCGUAUCGUAAGCAGUACUUU-X
Scr*	RNA	P-AGUACUGCUUACGAUACGGUU-X
GAPDH	DNA	F: CCATCACCATCTTCCAGGAGCGA R: GGTGGTGAAGACGCCAGTGGA
Myc	DNA	F: GCTCGTCTCAGAGAAGCTGG R: GCTCAGATCCTGCAGGTACAA
Anti-ctrl	LNA	TAACACGTCTATACGCCCA
Anti-l7	LNA	ACTATACAACCTACTACCTC
l7-6x	DNA	F:atcgccgtgtaattctagttgttAACTATACAAGGACTACCTCACCGG AACTATACAATGACTACCTCACCGGAAGTATACAAGGACTA CCTCACCGGAAGTATACAATGACTACCTCACCGGAAGTATA CAAGGACTACCTCACCGGAAGTATACAATGACTACCTCACC GGaaacgagctcgctagcctcgagtct R:agactcgaggctagcgagctcgtttCCGGTGAGGTAGTCATTGTATA GTTCCGGTGAGGTAGTCCTTGTATAGTTCCGGTGAGGTAG TCATTGTATAGTTCCGGTGAGGTAGTCCTTGTATAGTTCCG GTGAGGTAGTCATTGTATAGTTCCGGTGAGGTAGTCCTTGT ATAGTTaaacaactagaattacacggcgatc
ml7-6x		F:gatcgccgtgtaattctagttgttAACTATACAAGGACTAACGCACCG GAAGTATACAATGACTAACGCACCGGAAGTATACAAGGACT AACGCACCGGAAGTATACAATGACTAACGCACCGGAAGTATA

		<p>TACAAGGACTAACGCACCGGAACCTATACAATGACTAACGCA CCGGaaacgagctcgctagcctcgagtct R:agactcgaggctagcgagctcgtttCCGGTGCGTTAGTCATTGTATA GTTCCGGTGCGTTAGTCCTTGTATAGTTCCGGTGCGTTAGT CATTGTATAGTTCCGGTGCGTTAGTCCTTGTATAGTTCCGG TGCGTTAGTCATTGTATAGTTCCGGTGCGTTAGTCCTTGTA TAGTTaacaactagaattacacggcgatc</p>
L7-2x-cx-4x	DNA	<p>F:gggaattcAACTATACAAGGACTACCTCAccggAACTATACAA GGACTACCTCAccggaagtttcacaaagctaacaCCGGaagtttcacaaa gctaacaccggaagtttcacaaagctaacaggcggccgc R:gcgggccgcctgtagctttgtgaaaacttccggtgtagctttgtgaaaacttCCGGt gtagctttgtgaaaacttccggTGAGGTAGTCCTTGTATAGTTccggTG AGGTAGTCCTTGTATAGTTgaattccc</p>
FL-Q670 (smFISH)	DNA	<p>TCTTCGAGTGGGTAGAATGG TAGCGCTTCATGGCTTTGTG CGTCGGTAAAGGCGATGGTG GTAATGTCCACCTCGATATG CGAACGCTCATCTCGAAGTA ATAGCGCTTCATAGCTTCTG GATCCGATGGTTTGTATTCA AAGCTATTCTCGCTGCACAC CCAACACGGGCATGAAGAAC ACAGCCACACCGATGAACAG TTGTAGATGTCGTTAGCTGG CCTTTCTTGCTCACGAATAC TTGCACGTTGAGGATCTTTT TGGTAGTCGGTCTTGCTATC AGGTGTACATGCTTTGGAAG GGTGGCAAATGGGAAGTCAC CACGAAGTCGTA CTCTGTTGA ATGATCAGGGCGATGGTTTT CAATCCGGTACTGCCACTAC TGAATCGGACACAAGCGGTG ATGATCTGGTTGCCGAAGAT TGAAATGGCACCACGCTGAG AGCGTGGTGAACATGCCGAA AAAGCCGCAGATCAAGTAGC AAGCGGTACATGAGCACGAC AAGCTGCGCAAGAATAGCTC GCAGGGCAGATTGAATCTTA GAAGCTAAATAGTGTGGGCA TACTTGTCGATGAGAGTGCT ATCTCGTGCAAGTTGCTTAG</p>

CTGGTAGGTGGAAGCGTTTG
TTGTTTCTGTCAGGCCGTAG
CTTCGGGGGTGATCAGAATG
CACCTTAGCCTCGAAGAAGG
GTTACACCCAGTGTCTTAC
TTAACGTAGCCGCTCATGAT
GTCGATGAGAGCGTTTGTAG
CGGTCCACGATGAAGAAGTG
CTTGTATTTGATCAGGCTCT
ACATAGTCCACGATCTCCTT
AGCTTCTTGGCGGTTGTAAC
CTCGTCCACGAACACAACAC
TGAGAATCTCGCGGATCTTG

L941-Q670
(smFISH)

DNA

GACTGACTTCAGCCACGTC
CATAATGCTGCCGAGGAGC
CATCCGGCTCTCAGAAGTG
TCTGGACCTGGCTCCAAG
CTGAGAGGAGCCAGGATGG
CGCAGTTCAGAGAAGGCTA
TGTGGACCCGGGAGAAAAG
CCGGAGCGGTGGGAACTG
AAATCGCGGCGCACTGGG
ACTCTGGGGCTTGGACAC
TGGGGGTTGGTCTCAGAG
GAAGGCAGGAAGTCTGTGC
CTTTAGACACTTCTCGAGGG
GTTGTTTGGCTATCAACTGT
GCTTCTTTCATAATCAGTCA
CTGATTCTTGATAACAGTCT
GCTGAATGGTCAATGTCTGG
GTCTTTGTGCTGAATGTTCA
ATTCTGTGGGACTCTTCTGG
TTTTCTCTGAATAGTTTCCC
TTTGTATTGTCAGTATGCCT
GTCCACTACGTTAGAAGGAT
AAGATGGATACATGCTCCAG
TTGTGAAAGTGATCTCTGCT
CAATTCAAATCAAGAGCCCA
TGGATAGAGGGCTCATTACA
GAATCCAGTCAATTCGCAGA
GGCAGCAAGAATGAGAGTTG
AAGCATAGTTGGTCCATTGA
AGTGGTTATCATGTTATCCT

P: 5` Phosphate, X: 3` hydroxyl or C6 linker + Cy3 or C6 linker + Cy5

Table S2. Summary of dwell time quantifications from exponential fits.

Related to Figures 1-6. Figures S3-S4 and S6.

Construct	RNA	S/D*	T ₁ (s)	T ₂ (s)	T _{phb} (s)	T _w (s)
I7-Cy5/I7*	miRNA	D	0.5 ± 0.1	1.9 ± 0.6	2.3 ± 0.1	15
I7/I7*-Cy5	miRNA	S	-	1.1 ± 0.1	1.3 ± 0.1	15
ml7-Cy5/ml7*	miRNA	S	-	1.0 ± 0.2	1.3 ± 0.3	15
m21-Cy5/m21*	miRNA	D	0.6 ± 0.2	1.8 ± 0.3	2.1 ± 0.3	15
cx-Cy5/cx*	miRNA	S		1.5 ± 0.2	1.8 ± 0.1	15
scr-Cy5/scr*	miRNA	S		1.3 ± 0.1	1.5 ± 0.1	15
ml7-Cy5/ml7* + RL-I7-2x	miRNA+ mRNA	S	-	1.1 ± 0.2	1.3 ± 0.2	15
ml7-Cy5/ml7* + RL-ml7-2x	miRNA+ mRNA	D	0.4 ± 0.1	1.5 ± 0.2	1.7 ± 0.2	15
FL-I7-6x-MS2	mRNA	D	0.8 ± 0.1	4.9 ± 1.1	10.5 ± 1.7	15
FL-ml7-6x-MS2	mRNA	D	0.6 ± 0.2	2.3 ± 0.7	10.5 ± 1.7	15
I7-6x-FL-MS2	mRNA	D	0.5 ± 0.1	2.5 ± 0.5	10.4 ± 1.2	15
ml7-6x-FL-MS2	mRNA	D	0.6 ± 0.1	1.8 ± 0.3	10.9 ± 1.6	15
FL- MS2	mRNA	D	0.5 ± 0.1	2.1 ± 0.5	10.6 ± 2.0	15
FL-cx-6x-MS2	mRNA	D	0.4 ± 0.2	2.2 ± 0.1	11.4 ± 1.6	15
FL-I7-2x-cx-6x- MS2	mRNA	D	1.1 ± 0.3	4.8 ± 0.2	13.7 ± 2.1	15
THOR-MS2	lncRNA	D	0.4 ± 0.1	2.1 ± 0.6	9.6 ± 1.1	15
THOR-Δbs-MS2	lncRNA	S	0.1 ± 0.1		9.6 ± 1.1	15
ARlnc1-MS2	lncRNA	D	0.9 ± 0.2	2.3 ± 0.4	10.4 ± 1.4	15
L941-MS2	lncRNA	S	0.2 ± 0.1	-	11.2 ± 2.3	15

*Single exponential fit equation (S):

$$y = y_0 + A_1 \cdot e^{(-x/T_1)}; \text{ At } x = 0, y = y_0 + A_1$$

Double exponential fit equation (D):

$$y = y_0 + A_1 \cdot e^{(-x/T_1)} + A_2 \cdot e^{(-x/T_2)}; \text{ At } x = 0, y = y_0 + A_1 + A_2$$

T₁ = T_{fast}; T₂ = T_{slow}; T_{phb} = Photobleaching time; T_w = Acquisition window

Table S3. Summary of the number of cells, PBs / cell and RNAs / cell probed in this study.

Related to Figures 1-6 and Figures S1-S4 and S6.

RNA class	Name	Length	Live cell imaging			Fixed cell imaging		
			# Cells	# PB / Cell	# particles / Cell	# Cells	# PBs / Cell	# RNAs / Cell
miRNAs	l7-Cy5/l7*	22 nt	20	16	280	20	15	440
	l7/l7*-Cy5	22 nt	15	16	98	15	14	208
	ml7-Cy5/ml7*	22 nt	15	18	116	15	21	221
	ml7-Cy5/ml7* + RL-l7-2x	22 nt + ~1.2 kb	15	21	126	15	24	256
	ml7-Cy5/ml7* + RL-ml7-2x	22 nt + ~1.2 kb	15	17	254	15	18	381
	m21-Cy5/m21*	22 nt	15	23	232	20	20	372
	cx-Cy5/cx*	21 nt	15	23	128	20	21	225
	scr-Cy5/scr*	21 nt	15	27	65	20	26	193
mRNAs	FL-MS2	~3.2 kb	20	14	311	20	12	398
	FL-cx-6x-MS2	~3.4 kb	20	16	298	20	18	312
	FL-l7-2x-cx-6x-MS2	~3.4 kb	20	21	152	20	23	148
	FL-l7-6x-MS2	~3.4 kb	20	20	108	20	29	151
	FL-ml7-6x-MS2	~3.4 kb	20	11	247	20	12	219
	l7-6x-FL-MS2	~3.4 kb	20	14	113	20	13	108
	ml7-6x-FL-MS2	~3.4 kb	20	18	204	20	19	243
lncRNAs	THOR-MS2	~ 2.3 kb	20	22	141	20	23	203
	THOR-Δbs-MS2	~ 2.1 kb	30	21	122	15	22	102
	ARlnc1-MS2	~4.2 kb	20	18	195	15	21	275
	L941-MS2	~3.4 kb	30	17	228	15	17	208